Helsinki University of Technology
Department of Electrical and Communications Engineering
Laboratory of Electronics Production Technology
Espoo 2005

RELIABILITY OF HIGH–DENSITY LEAD–FREE SOLDER INTERCONNECTIONS UNDER THERMAL CYCLING AND MECHANICAL SHOCK LOADING

Toni Mattila

Dissertation for the degree of Doctor of Science in Technology to be presented with due permission of the Department of Electrical and Communications Engineering, Helsinki University of Technology, for public examination and debate in Auditorium S2 at Helsinki University of Technology (Espoo, Finland) on the 16th of December, 2005, at 12:00.

SUPERVISOR

Professor Jorma Kivilahti, D. Sc. (Eng.)
Department of Electrical and Communications Engineering
Laboratory of Electronics Production Technology

REVIEWERS

Professor Matti Korhonen, D. Sc. (Eng.)
Cornell University
Materials Science & Engineering
Ithaca, United States of America

Senior Engineering Manager Luu Nguyen, Ph. D.
National Semiconductor Corporation
Santa Clara, United States of America

OPPONENTS

Professor Matti Korhonen, D. Sc. (Eng.)
Cornell University
Materials Science & Engineering
Ithaca, United States of America

Senior Specialist Olli Salmela, D.Sc. (Tech.)
Nokia, P.O. Box 301, 00045 Nokia Group
Nokia, Linnoitustie 6, 02600 Espoo

Distribution:
Helsinki University of Technology
Department of Electrical and Communications Engineering
Laboratory of Electronics Production Technology
P.O. Box 3000
FIN-02015 HUT, Finland
Tel: +358 (0)9 451 2716
Fax: +358 (0)9 451 5776
E-mail: Pia.Holmberg@hut.fi
www.ept.hut.fi

HUT-EPT-13
ISSN 1457-0440
ISBN 951-22-7983-5 (printed)
ISBN 951-22-7984-3 (PDF)

Otamedia Oy
Espoo 2005

ABSTRACT

The reliability of portable electronic devices was studied by applying standardized test procedures for test vehicles that represent the technologies and lead-free materials typically used in novel portable products. Thermal cycling and drop testing are commonly used because they reveal the failure modes and mechanisms that portable devices experience in operational environments. A large number of component boards were assembled in a full-scale production line to enable proper statistical and fractographic analyses. The test boards were assembled with different printed wiring board protective coatings, component under bump metallizations, and solder pad structures. The component boards were tested and the times-to-failure of the various combinations were statistically analyzed. The reliability data were also analyzed by the Weibull method, and the characteristic lifetimes and shape parameters were calculated.

The failure modes under the thermal cycling, where solder interconnections fail by cracking through the bulk solder, were different from those observed in the drop tests, where cracks propagate along the intermetallic layers on either side of the interconnections. Under the thermomechanical loading the as-soldered microstructure, which is composed of only a few large eutectic colonies, undergoes local recrystallization that produces networks of grain boundaries along which the intergranular cracks damage solder interconnections. Under the mechanical shock loading, in turn, the strain–rate hardening of the solder material forces cracks to propagate in the intermetallic layers instead of the bulk solder.

It was found that the reliability of solder interconnections can improve when the component boards have undergone thermal cycles before drop testing. The high-angle boundaries between the recrystallized grains generated during thermal cycling provide paths along which cracks can propagate but the propagation through the bulk solder consumes more energy than the propagation through brittle intermetallic layers. On the other hand, prolonged lifetime at elevated temperatures can reduce the drop test reliability considerably due to the formation of Kirkendall voids in the Cu_3Sn intermetallic layers.

PREFACE

The work for this thesis has been carried out at the Department of Electrical and Communications Engineering at the Helsinki University of Technology. I am most grateful to my supervisor professor Jorma Kivilahti for his guidance, time and support. I have always admired and appreciated his enormous enthusiasm to understand everything as precisely as possible. His persistency has constantly helped me to improve myself.

I wish to thank the co-authors Dr. Tomi Laurila, Pekka Marjamäki, and Vesa Vuorinen for their contribution and willingness for discussion at any time. I am also grateful to all my co-workers Dr. Kari Lounatmaa, Dr. Markus Turunen, Pia Holmberg, Hanna Järvelä, Pirjo Kontio, Ari Kuisma, and Tuomas Waris for their contributions towards the completion of this work.

The financial support from the National Technology Agency of Finland (TEKES), Aspocomp Group, Atotech GmbH, Elcoteq SE, Micro Analog Systems Oy, and Nokia Group is greatly acknowledged.

Finally, I would like to thank my fiancée, Tanja, for her endless love and support. My parents deserve special thanks for providing continuous encouragement and support throughout my life.

Espoo, December 2005
Toni Mattila

Contents Page

List of Publications

Appendix I — T. T. Mattila, V. Vuorinen, and J. K. Kivilahti, "Impact of printed wiring board coatings on the reliability of lead–free chip–scale package interconnections", *Journal of Materials Research*, **19**, 11, (2004), pp. 3214–3223.

Appendix II — T. T. Mattila, P. Marjamäki, and J. K. Kivilahti, "Reliability of CSP interconnections under mechanical shock loading conditions", *IEEE Transactions on Components and Packaging Technologies*, (in print).

Appendix III — T. T. Mattila and J. K. Kivilahti, "Failure mechanisms of lead–free chip scale package interconnections under fast mechanical loading", *Journal of Electronic Materials*, **34**, 7, (2005), pp. 969–976.

Appendix IV — T. T. Mattila and J. K. Kivilahti, "Reliability of lead–free interconnections under consecutive thermal and mechanical loadings", *Journal of Electronic Materials*, (in print).

Appendix V — T. T. Mattila, T. Laurila, and J.K. Kivilahti, "Metallurgical factors behind the reliability of high–density lead–free interconnections", in E. Suhir, C. P. Wong, and Y. C. Lee, *Micro- and Opto-Electronic Materials and Structures: Physics, Mechanics, Design, Reliability, Packaging*, Springer Publishing Company, (in print).

The research program was planned and the theoretical aspects, as they appear in the manuscripts, were discussed by the author together with co-author J. K. Kivilahti. The author assembled the component boards on an SMT production line and carried out the reliability testing, the statistical analyses, and the failure analyses. The author wrote the manuscripts, which have been discussed in detail with the co-authors. The finite element calculations were carried out by co-author P. Marjamäki and the thermodynamic calculations by the co-author V. Vuorinen. Co-author T. Laurila provided discussion on interfacial reactions.

1. INTRODUCTION

Electronics manufacturers have been successful in making ever smaller and lighter weight portable products equipped with an increasing number of functions. This development has been facilitated by the adoption of surface mount technology (SMT), which is a reasonably low–cost solution for the production of small–scale, high–density portable products. SMT–based chip–scale packages (CSP), which enable good electrical performance and large–scale integration, are utilized in most portable equipment on the market today. However, increasing interconnection densities, decreasing interconnection volumes, and growing complexity of solder metallurgies create considerable reliability challenges. Because the finer pitch components are placed closer to the printed wiring boards (PWB), solder interconnections experience considerably increased strains and stresses.

The adoption of new lead–free materials gives rise to a variety of reliability concerns. In particular, challenges are associated with the increasing complexity of solder metallurgies, as new combinations of solder pastes, PWB protective coatings, and component terminal metallizations produce unforeseen microstructures and defects in increasingly smaller solder interconnections. Tin–lead alloys have conventionally been used to make the solder connections between component I/Os and printed wiring boards, but banning the use of lead for health reasons is now under worldwide discussion. A recent EU directive, effective July 1st, 2006, will restrict the use of lead in electronic products sold in EU markets to below 0.1 wt-% or above 85 wt-% in homogeneous material [1-3]. The use of lead in high melting temperature solders is allowed until further notice because no suitable replacement has yet been found.

The easiest way to comply with the requirement would be to remove lead altogether and use tin as solder. However, owing to its high melting point (T_{mp}(Sn) = 232 °C) and inadequate mechanical properties, tin alone cannot be used in volume production. Most lead–free solder candidates are based on tin with one or two but sometimes even more alloying elements [4-33]. Tin–lead solders are being replaced with alloys such as Sn3.8Ag0.7Cu [8-16], Sn3.5Ag3.0Bi [17-21], Sn3.5Ag [22-27], Sn0.7Cu, or SnBi-based alloys [28-33]. At the time of writing, SnAgCu is considered the most promising

candidate for general–purpose replacement of tin–lead in SMT reflow processes [34,35]. Further development in the flux technology is needed, however. Similarly, bare copper PWB soldering pads or copper as component terminal metallization is hardly ever used due to the oxidation of copper at room temperature under atmospheric conditions. Thus, lead–free protective coatings such as nickel–phosphorous–gold (Ni(P)|Au) or organic soldering preservative (OSP) will be required on PWB copper soldering pads, while protective metallizations such as Ni|Au, Ni(V)|Cu, Ni|Pd|Au, and Sn will be used on the component side. The solder alloys together with the contact metals form interconnections whose microstructures greatly affect the reliability of soldered assemblies. It is of paramount importance, therefore, to investigate the impact of interconnection microstructures on the reliability with component boards assembled as the commercial products are assembled in volume production.

The growing complexity of solder interconnection metallurgies increases the importance of reliability testing. However, longer testing time adds to the cost of new products not only due to the direct expenses related to testing but also due to the longer times to market. The employment of correct test procedures for particular applications is thus critically important. Portable electronic products encounter diverse environments in ordinary daily use and therefore their reliability should be studied with tests that simulate real–use strains and stresses as realistically as possible. Portable electronic products are exposed to temperature fluctuations due either to internally generated heat dissipation or to the external operational environment, but they are especially prone to failure due to mechanical shock loads caused by dropping. These loadings are simulated with standardized reliability tests that also allow comparative studies of different material combinations. Studying the different loadings independently gives, of course, an incomplete understanding of the failure mechanisms in real–use environments. Portable products are seldom dropped soon after they are assembled. More likely they have experienced some thermomechanical loading and have been exposed to elevated temperatures before they are dropped. Taking into account the microstructural changes in solder interconnections due to normal operation requires that different reliability tests be combined. Moreover, to ensure the feasibility of the test results, a good understanding of the failure mechanisms occurring under the different loading conditions must be obtained

first. Thus, because different material combinations have different lifetimes under a certain loading, and because different loadings evoke different failure mechanisms, the reliability must be studied systematically by involving both physics–of–failure and statistical approaches. Statistical methods are needed for study of the failure–rates and to classify the failure modes, as well as to make inferences regarding differences in lifetimes under tests.

In this thesis the reliability of chip–scale packaged components was investigated under cyclic thermomechanical and mechanical shock loadings. Thermal cycling was carried out according to the IEC standard 68-2-14N and drop tests according to the JEDEC standard JESD22-B111. The CSP component and the PWB protective coatings were the same in all of the papers included in the appendixes. The component was a lead–free SnAgCu–bumped ball grid array and the test boards were assembled using near–eutectic SnAgCu solder pastes. Two PWB protective coatings, Ni(P)|Au or OSP, were used on the copper soldering pads. The availability of a large number of test structures assembled in a full–scale production line enabled comprehensive statistical analysis of the reliability test results. Statistical significance testing and the Weibull method were employed. Detailed microstructural investigations were carried out to reveal the failure modes in the different material combinations and failure mechanisms under the two reliability tests.

Chapters 2 and 3, in the following, provide a discussion of the physical properties of SnAgCu solder interconnections and their response to loading. The statistical methods applied in this thesis are discussed in chapter 4. Chapter 5 summarizes the findings of the studies, which are reported in detail in the five appended publications.

2. PHYSICAL PROPERTIES OF SOLDER INTERCONNECTIONS

The reliability of portable electronic products has been studied extensively over the years, and very often the electrical failures have been associated with cracking of solder interconnections. The adaptation of new component technologies and lead–free materials has not changed the situation. The mechanical integrity of solder

interconnections is largely determined by the response of solder interconnections to loading. Solder accommodates strains and stresses by deforming plastically. In the course of time, plastically deformed interconnections undergo changes in microstructure. The evolution of interconnection microstructures, on the other hand, affects the mechanisms by which interconnections fail. Therefore, in this chapter plastic deformation, restoration, and fracture of solder interconnections are discussed. The response of solder interconnections to different loading types, namely cyclic thermomechanical and mechanical shock loading, will be discussed in chapter 3.

2.1 Plastic Deformation of Solders

Deformation of materials can be presented by stress–strain diagrams where the elastic and plastic behaviors are differentiated by the yield stress (σ_y). At stress levels equal to or higher than the yield stress, deformation is not recoverable upon release of stress and the material is deformed plastically. When loading is carried out above the yield stress, the load typically has to be increased for additional strain to occur. This effect is called strain hardening and is associated with increase in the number of defects in the material caused by plastic deformation. Any stress above the yield stress is termed flow stress.

The conventional plastic flow of materials occurs by two primary mechanisms: dislocation slip and/or climb, and twinning. The dislocation slip is parallel displacement of two adjacent crystal regions relative to each other by movement of dislocations across a specific, usually close–packed, slip plane or set of planes. Slip does not occur on just one plane but over small regions of parallel planes called slip bands. The combination of slip planes and directions defines a slip system. Because the near eutectic SnAgCu solders are particularly high in tin, their plastic behavior is dictated by the deformation characteristics of tin. Tin has a highly asymmetric body centric tetragonal structure (a = b = 5.8314 nm, c = 3.1815 nm at 25 °C [36]) and has relatively many different types of slip systems as compared with cubic structures. The known operative slip systems of tin are (110) [001], (100) [001], $(10\bar{1})$ [101], and (121)[101] [37]. Slip will take place only when the resolved shear stress (σ_{RSS}) of the slip plane increases above a critical value.

The critical shear stress for tin single crystals, when the stress is applied in the [001] direction, is 0.9 kg/mm^2 [38]. SnAgCu interconnections are polycrystalline but consist of only a few large grains, as will be discussed later on. In polycrystalline materials, slip appears first in grains where orientation of the slip plane results in the highest resolved shear stress. If a material, such as tin, possesses a small number of operative slip systems, the temperature is very low, or the strain rate is very high, the twinning mechanism may be activated to provide means for additional deformation. Twinning is defined as a region of a crystalline body that has undergone homogeneous shape deformation in such a way that the resulting structure is identical with that of the parent, but oriented differently [39]. A twinned structure is a symmetrical arrangement of atoms across a common plane. The two regions have identical crystal structures, but the atom positions in the twin are a mirror image of those of the original structure. The known twinning planes and directions of tin are $\{301\}<\bar{1}03>$ and $\{101\}<10\bar{1}>$ [40].

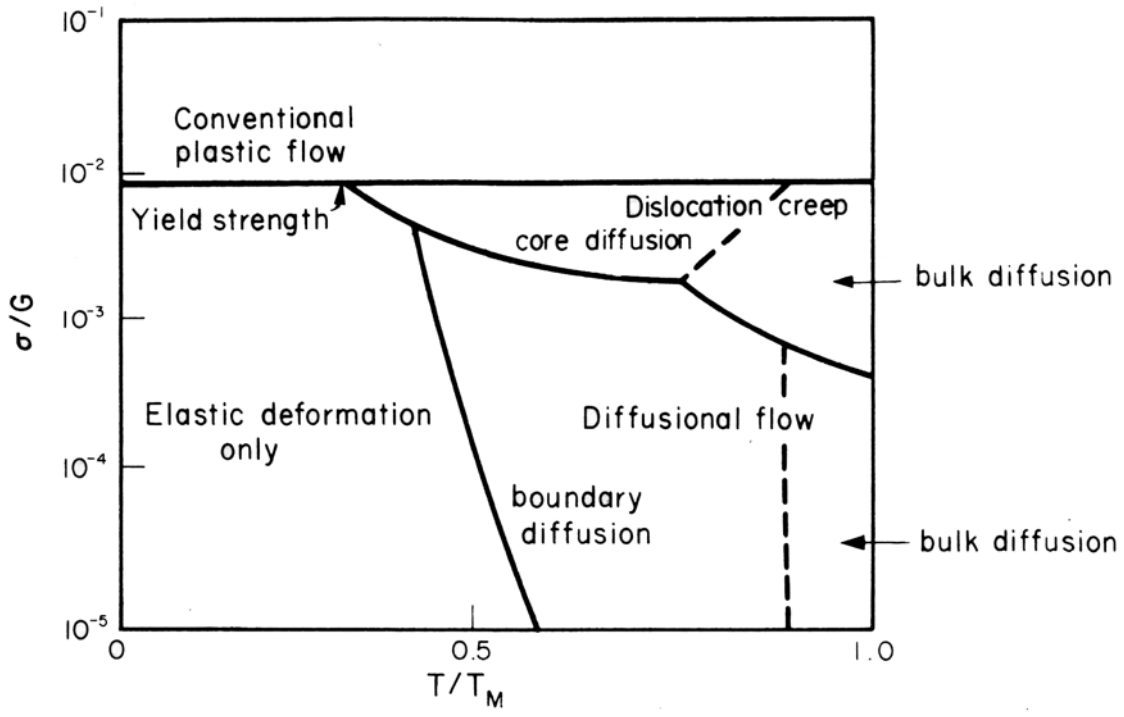

Figure 1: *Deformation mechanisms at different stresses and temperatures (reprinted from ref. 41 with kind permission from Elsevier).*

The classification of deformation behavior as elastic when the applied stress is below the yield stress and plastic when the applied stress is above it is valid only at low homologous temperatures. The homologous temperature is defined as the ratio of the prevailing temperature (T) to the melting point of a material (T_m) expressed in absolute temperature scale. Figure 1 shows a deformation diagram indicating the regions in which the different mechanisms operate. Applied shear stress is divided by the shear modulus of a material (G), and homologous temperature is used instead of absolute temperature in order to treat different materials equally. The presentation is simplified because it is well known that the yield strength of metals decreases with increasing temperature and the boundaries between the different mechanisms are not exact. As shown in Figure 1, below the homologous temperatures of about 0.3 - 0.4 yield strength divides the deformation of a material into elastic and plastic regions as a function of applied stress. At low temperatures, dislocations move along and cross–slip between the slip planes; while nonconservative motion is restricted. On the other hand, at homologous temperatures above 0.3 to 0.4, say 0.45, nonconservative motion of dislocation becomes possible because the diffusion of vacancies (and interstitial atoms) becomes faster. Therefore, at high homologous temperatures plastic deformation becomes time–dependent and materials can be deformed plastically even at stress levels below their macroscopic yield stress. This phenomenon is called creep, and it can be defined as time–dependent plastic deformation of a material [42].

Two main types of deformation mechanisms act at stresses below the macroscopic yield strength of a material at homologous temperatures above 0.3 - 0.4: dislocation creep and diffusional flow. Stress levels above the critical shear stress enable the movement of dislocations, and the dislocation creep mechanisms become active. However, the rate–controlling process in the high temperature creep of metals is the climb of dislocations having an edge component to overcome an obstacle on the slip plane [42]. These obstacles include solute atoms, precipitates, inclusions, and other dislocations. To overcome such obstacles, dislocations must be able to move in a direction perpendicular to the slip plane, but this requires diffusion. At higher homologous temperatures bulk diffusion is the dominant mechanism whereas at lower temperatures it is the core diffusion. In core diffusion, atoms and vacancies diffuse in the

core of an edge dislocation, whereas in bulk diffusion they travel through the crystal lattice. After the obstacle has been overtaken, further slip can take place until another obstacle is encountered. Andrade's law describes the creep strain under constant stress and temperature:

$$\varepsilon = \varepsilon_e + \varepsilon_p + \beta t^n + Kt,$$

where ε_e is the elastic strain, ε_p is the instantaneous plastic strain, t is time, and n, β, and K are material constants [42]. K determines the temperature (T) dependency of the creep strain and it can be presented with the Arrhenius relation $K = K_0 \exp(-Q/kT)$, where K_0 is a constant, Q is the activation energy of creep, and k is Boltzmann's constant.

At stresses below the critical shear stress, plastic deformation cannot take place by the movement of dislocations and, instead, it takes place by diffusion. Under an applied stress, creep occurs through grain elongation, which is the result of diffusion of vacancies (and atoms in the opposite direction) from grain boundaries undergoing tensile stress to boundaries undergoing compression. This migration can take place either through the crystal lattice of the grain (Nabarro–Herring creep) or along the boundaries of the grain (Coble creep). Grain boundary sliding is typically accompanied by these mechanisms to balance the mass flow due to diffusion.

Furthermore, plastic behavior of metals can be strain–rate dependent: in general, strength increases with strain rate. According to Johnston and Gilman [44] the plastic strain rate is given by $\dot{\varepsilon} = b\rho v$, where b is the length of the Burgers vector, ρ is the number of dislocations per unit, and v is the average dislocation velocity. Velocity is highly sensitive to the applied stress because it increases exponentially as a function of stress [45]. However, there is an upper limit for the velocity of dislocations. It asymptotically approaches the velocity of shear waves, i.e. the speed of sound in the medium, but any defects, alloying elements, or impurities decrease it. The average number of dislocations thus has a significant effect on the strain–rate sensitivity of metals under high deformation rates. Propensity towards twinning has been found to increase with higher strain rates, especially with metals having relatively few slip systems. Thus, twinning provides an additional mechanism for deformation under high strain rates.

2.2 Restoration of Plastically Deformed Structures

Structures formed in solder interconnections during plastic deformation are unstable and are gradually restored. Restoration can take place either during deformation (dynamic restoration) or at elevated temperatures after deformation (static restoration). The restoration of plastically deformed interconnections proceeds mainly by two mechanisms: recovery and recrystallization. *Recovery* occurs without notable change in the grain structure, but changes involving *recrystallization* are clearly visible even with the resolution of an optical microscope. Recovery and recrystallization are competing restoration processes, but recovery typically precedes recrystallization. Restoration is typically followed by uniform *grain growth* or highly selective *secondary recrystallization*.

When solder interconnections are deformed plastically, energy is stored in the crystal lattice in the form of defects such as vacancies, interstitial atoms, stacking faults, dislocations, and deformation twins. The purity of the bulk solder, the amount of deformation, temperature, and grain size affect the amount of stored energy, but measurements have shown that about 1–15% of the energy consumed in causing the deformation is stored in the structures, and the rest is dissipated irreversibly as heat [46]. If the solder alloy is subsequently heated, physical properties such as yield strength, hardness, ductility, resistivity, and density are gradually restored towards their values before the deformation. The driving force of this restoration process is the release of energy trapped in the material during deformation. Dislocations and vacancies are the two most important defects produced during deformation. Since the vacancies account for only a small fraction of the total energy stored, movement of dislocations governs the recovery processes of solder interconnections. The process of restoration, grain growth, and some of the related property changes are illustrated in Figure 2. The degree of restoration by recovery depends on the stacking fault energy of the material. The dissociation of dislocations is not energetically feasible in materials with high stacking fault energy. Therefore, when dislocations remain undissociated they can climb and cross–slip, and the decrease of the energy stored in the deformation structures takes place by recovery.

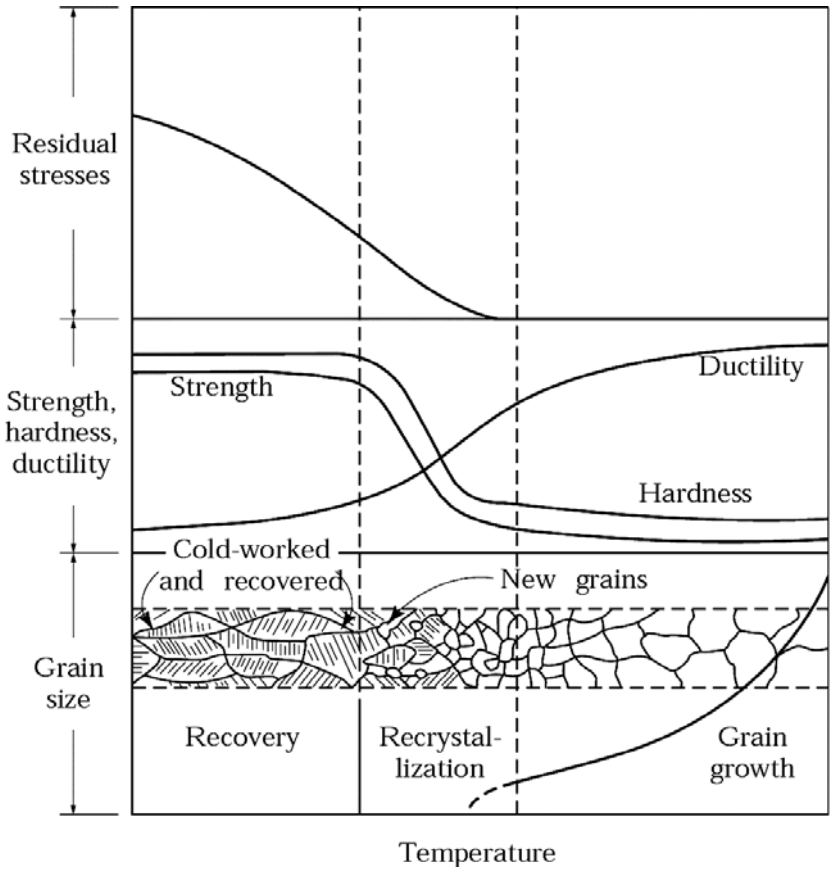

Figure 2: *Restoration of mechanical properties to values before deformation (reprinted from ref. 47 with kind permission from McGraw-Hill Companies).*

At the time of writing there is little information in the literature about the recrystallization behavior of Sn–based lead–free solders. However, since the near eutectic SnAgCu alloy contains more than 95 wt-% of Sn, recrystallization studies on pure Sn can be considered indicative, bearing in mind that the alloying elements do affect the restoration processes. Restoration studies carried out with high–purity tin have suggested that the stacking fault energy of tin is high [48,49], and thus restoration takes place to a large extent by recovery; however, other studies have shown that Sn (99.995% purity) recrystallizes at room temperature even after slight deformation (reductions of a few percent) [50]. Guy [51] has measured recrystallization temperatures for several metals, and for Sn he obtained the value of – 3 °C. It should be emphasized that this value refers to a temperature at which a highly deformed (tens of percent reduction) alloy

recrystallizes completely in one hour. The word “highly” is important because the degree of deformation affects the temperature necessary to onset recrystallization. The recrystallization temperature of solder interconnections will be different from the above because even small additions of soluble alloying elements raise the recrystallization temperature of the base metal but near eutectic SnAgCu alloys are, however, known to recrystallize during typical thermal cycling between – 45 ºC and + 125 ºC [52-55]. Since both recovery and recrystallization take place in the restoration of deformed solder interconnections, the characteristics of both will be briefly discussed in the following.

The restoration of mechanical properties by **recovery** typically takes place only to about one fifth of the fully annealed value [56]. There are many different mechanisms and the order of their occurrence reflects the thermal activation required. At low temperatures, coalescence of point defects and migration of the defects to grain boundaries or dislocations take place. As the temperature is increased, dislocation–based mechanisms begin to operate. Dislocation tangles start forming dislocation sub–grain networks. The interiors of the sub–grains have relatively low dislocation densities, while density at the (small–angle) sub–grain boundaries is still high. Sub–grain boundaries move, and dislocations enclosed within the boundaries merge into the boundaries. As a result, the sub–grain boundaries sharpen as the dislocations are annihilated or rearranged into stable configurations by climbing.

At higher temperatures most solders undergo a discontinuous change in grain structure known as **recrystallization**. In this process, new strain–free crystals are formed within the deformed microstructures, and the new crystals grow in size consuming the deformed grains until they disappear. Since recovery and recrystallization are competing processes and the activation energy of recovery is smaller than that of recrystallization, recovery takes place before recrystallization and the progress of recovery decreases the driving force for recrystallization. Therefore there is also a critical level of deformation (critical reduction) below which recrystallization does not take place. After an incubation period, strain–free grains begin to nucleate at numerous locations simultaneously. The nucleation of new grains takes place in areas where the microstructure has been most severely damaged, such as at grain boundaries (preferentially at a high–angle triple point) or near free surfaces. There is a critical size below which a cluster of atoms cannot form a

stable nucleus, but once a nucleus is formed the newly formed grains grow by motion of the boundary between the stable recrystallized grain and the strained matrix until further growth is suppressed by the adjacent (newly formed) grains [57]. Impurities and second–phase particles are thus pushed to the boundaries between the newly crystallized grains.

The rate at which the primary recrystallization takes place is a function of both the nucleation rate and the growth rate of the newly formed crystals. The kinetics of recrystallization is also dependent on time and temperature. *Avrami's equation* describes the isothermal recrystallization kinetics with the relation

$$\zeta = 1 - \exp(-Kt^n),$$

where ζ is the crystalline volume fraction developed at time t, K is a temperature dependent constant, and n is a constant dependent on the nature of nucleation and growth [58]. Parameter K is constant in isothermal conditions but is exponentially dependent on temperature and the relation can be presented by the Arrhenius equation $K = K_o \exp(-Q/(kT))$, where K_o is a constant and Q represents the activation energy of crystallization.

The type of microstructure formed at the end of recrystallization depends on the nucleation rate (N) and growth rate (G): the greater the nucleation rate relative to the growth rate, the finer the ultimate grain size. Both N and G are affected by several factors. Gorelik has presented a good summary of them [59]. An increase in annealing temperature, amount of deformation, or rate of deformation increases both N and G, and the rate of recrystallization is thereby increased. But the increase in N is generally larger than that in G and therefore finer grain size will result after recrystallization. The final grain size is chiefly dependent on the degree of deformation and to a lesser extent on the annealing temperature. Dispersed precipitates such as second–phase particles present in the matrix increase N and decrease G, especially if the second–phase particles are comparatively large. Large precipitates enhance the inhomogeneity of deformation by acting as barriers on which dislocations accumulate [57,60]. This shortens the incubation time of recrystallization. Furthermore, these inclusions inhibit boundary migration and thus suppress the growth of recrystallized grains.

The recrystallized grains grow in size until they begin to collide with one another and there is no deformed structure left to consume. This is the end of primary recrystallization, but continued heating causes the grains to grow further at the expense of the neighboring recrystallized grains. This effect is known as **grain growth**, which is defined as a gradual increase in the average grain size after all the deformed grains have been consumed by the new strain–free grains. During grain growth, individual grains grow exaggeratedly but they do not grow in some preferred direction. **Secondary recrystallization** can also be described as exaggerated grain growth, but it differs from the grain growth in the sense that in secondary recrystallization grains grow non–uniformly. The driving force for both grain growth and secondary recrystallization is the decrease in grain boundary surface energy associated with the decrease in the total area of grain boundaries.

2.3 Fracture Modes and Mechanisms in Solder Interconnections

The mechanism by which solder interconnections fail depend on the loading conditions and the same fracture mechanism may evoke different fracture modes. The fracture mechanism tells how cracks nucleate and develop, whereas the fracture mode describes the fracture. The fractures of solder interconnections can be either ductile or brittle, the difference being defined in terms of the energy required for fracture, i.e. the fracture toughness. A ductile fracture is a high–energy fracture because a relatively large amount of energy is absorbed due to the plastic deformation occurring during fracture. Brittle fracture is a low–energy fracture because cracks propagate with little or no plastic deformation. The tendency towards brittle fracture is increased at low temperatures and high strain rates. The basic fracture mechanisms, microvoid coalescence and fatigue fracture, are discussed in the following.

2.3.1 Microvoid Coalescence

Tin has been observed to fail by void coalescence at the grain boundaries at elevated temperatures (190 °C) when stressed uniaxially under a constant load [61]. The

fracture mechanism of **microvoid coalescence** is characterized by nucleation of microvoids and their growth and coalescence to form cracks. The nucleation of voids due to plastic straining is typically attributed to either particle cracking, interfacial decohesion between a particle and the surrounding matrix, or decohesion between grains. As the deformation continues, these voids enlarge, which consumes most of the energy required for fracture. The final step of the fracture mechanism is coalescence of the numerous voids in the direction of maximum shear stress and necking down of the ligaments between adjacent microvoids, resulting in the formation of localized cracks. The cracks propagate slowly because they only extend when additional stress is applied. The resultant fracture surface is of highly irregular appearance, and the size of the dimples visible on the fractured surfaces may vary widely because nucleation of microvoids depends on several different factors (inclusion size, stress and strain levels, the amount of deformation, purity of the material, for instance). Microvoid coalescence is a typical failure mechanism of ductile fracture.

2.3.2 Fatigue Fracture

When solder interconnections are subjected to repeated loading they can fracture even at stress levels below the yield strength, due to fatigue. The classical fatigue failures typically occur suddenly and unexpectedly because observable (macroscopic) plastic deformation does not occur before failure. Although solder interconnections under thermomechanical loading also fail by fatigue, the failure mechanism differs from the classical fatigue failure mechanism because plastic deformation precedes crack nucleation and propagation. High tin solder interconnections fail under thermomechanical loading by recrystallization–induced fatigue fracture, where the cracks nucleate and grow along the grain boundaries of the recrystallized grains.

a) Fatigue Fracture at Room Temperature

When stressed cyclically at room temperature with frequencies in the range of 10^{-3} to 10 Hz, solder interconnections fail by cracking through the bulk solder with little

regard to their microstructures [62-65]. Fatigue failure is a three–stage process involving crack nucleation, crack growth, and final failure. When defects or cracks are pre–existent, the nucleation stage is shortened or omitted entirely, and the number of cycles to failure is reduced. The fatigue cracks grow slowly with increasing number of load cycles until the component fails.

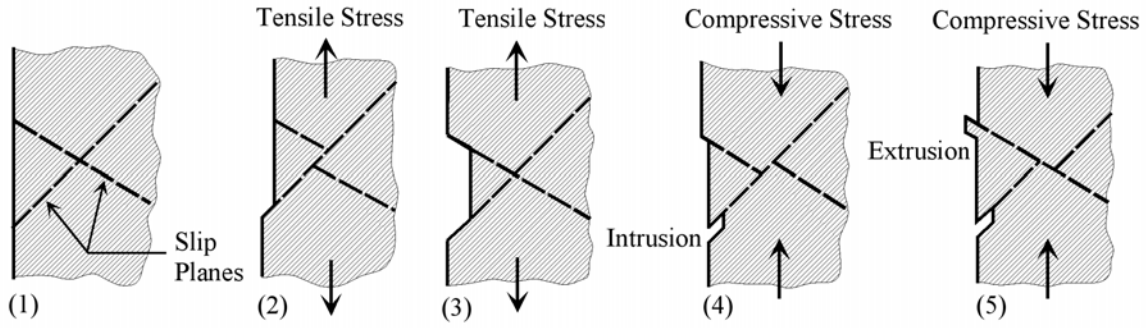

Figure 3: *Nucleation of fatigue fracture by plastic deformation on a surface*

Fatigue cracks nucleate preferentially at scratches, notches, dents, or wherever stresses can concentrate on the surface of a material. If suitable pre–existent sites for crack nucleation are not available, plastic deformation will produce intrusions and extrusions on the surface of the material by the mechanism illustrated in Figure 3. This micro–plasticity occurs preferentially at the surface of a material because the material is constrained everywhere else. Slip deformation, typically when concentrated on only a few slip planes, can cause surface discontinuities such as intrusions and extrusions, which provide suitable places for cracks to nucleate. The first nucleation site of a microcrack is therefore along the slip bands. The growth of a newly nucleated crack is oriented along a plane at an angle of about 45° to the axis of stressing because this is, according to Schmid's law, the direction of most favorably oriented slip planes. After a relatively short distance the orientation of cracks changes to that determined by the relative stress state. The crack nucleation period is considered complete when the crack growth is no longer dependent on the structure of the deformed surface.

Tensile stress produces a plastic zone at the tip of the crack and makes the crack tip stretch plastically by a finite length. The plastic deformation taking place at the tip of the crack does not cause recrystallization, even if the minimum required deformation is

exceeded, because the kinetics of recrystallization at room temperature is too slow. In most environments an oxide layer very quickly covers the surface of this fresh material at the tip of the crack. The following compressive cycle pushes the crack shut, making the new surface fold forward. This same mechanism repeats on every cycle and the crack propagates on each cycle until the material fails completely. Any inclusions within the plastic zone at the tip of the crack enhance the growth rate. When the cracks grow by a small amount each cycle, striations characteristic for fatigue fracture are produced on the fractured surfaces. At a certain stage in the growth of a fatigue crack, the area of the uncracked cross–section will be reduced to a point where the stress acting on the remaining surface reaches a level at which an ordinary brittle or ductile fracture can occur.

b) Fatigue Fracture during Thermal Cycling

Under thermomechanical loading, high–tin solder interconnections undergo local recrystallization that produces networks of grain boundaries along which cracks can nucleate and propagate. A crack propagating along grain boundaries is termed an **intergranular fracture**. The microstructure of the fractured material is reflected in the morphology of the fracture surface. Impurities, alloying elements, or second–phase particles that are left on the grain boundaries of recrystallized grains promote intercrystalline cracking. Impurity and alloying elements at grain boundaries decrease the cohesion between adjacent grains, whereas inclusions and second–phase particles facilitate microcrack nucleation and cavity formation at grain boundaries.

When the grain growth or secondary recrystallization has coarsened the microstructures of high–tin interconnections, fracture can take place by a mixed mode of intergranular and transgranular fracture [66]. The **transgranular** fracture (i.e. cleavage fracture) takes place by cracking of atomic bonds along crystallographic planes. The transgranular crack propagates through the grains until it transverses a grain boundary, where the crack plane reorients its direction in search of suitable crystallographic planes in the new grain. Transgranular fracture leaves a facetted appearance on the fracture

surface and is typically bright and shiny. This fracture mechanism requires less energy than the mechanism of microvoid coalescence because very little plastic work is required.

3. RELIABILITY TESTING OF COMPONENT BOARDS UNDER THERMOMECHANICAL AND MECHANICAL LOADINGS

Thermal cycling tests are used to simulate the effect of thermal changes, caused by ambient environment or heat dissipating components, on the reliability of electronic assemblies. The various materials of component boards have dissimilar coefficients of thermal expansion (CTE), so that changes in the temperature of the product produces thermomechanical stresses that ultimately cause the assemblies to fail by fatigue. The severity of the thermal cycling tests is essentially determined by the values of upper and lower temperatures and the amount of time allowed for the thermomechanical strains to relax. While the reliability of portable electronic products is threatened by thermomechanical loading, it may be even more severely threatened by mechanical shock loads when products are dropped on the ground. The effect of mechanical shock impacts is studied with tests where component boards are dropped repeatedly in order to produce a desired shock impact on the test assembly.

3.1 SnAgCu Interconnections Under Thermomechanical Loading

Thermal cycling is a typical example of a strain–controlled cyclic loading, where the temperature range and the CTEs of adjoining materials dictate the level of stresses produced in a structure. For instance, the CTE of FR–4, which is a typical base material of PWBs, is about 16 x 10^{-6}/°C [67] whereas that of silicon is only 2.5 x 10^{-6}/°C [68]. This difference in CTEs is called thermal mismatch and it is primarily accommodated by deformation of the solder interconnections because the strength of the solder interconnections is low compared with that of the component and substrate materials. The total amount of strain produced is the result of thermal mismatch at different scales: a) on a macroscopic scale between printed wiring board and components, b) on an intermediate

scale between solder and contact metals, and c) on a microscopic scale between different phases or grains of the interconnections. In addition to the magnitude of thermal change (ΔT) and the difference in the CTEs ($\Delta\alpha$), the extent of deformation ($\Delta\gamma$) depends on the structure of the component, namely the height (h) of solder interconnections and the distance of interconnections from the neutral point (L). Their relation can be presented by the equation $\Delta\gamma = \Delta\alpha \times \Delta T \times L / h$.

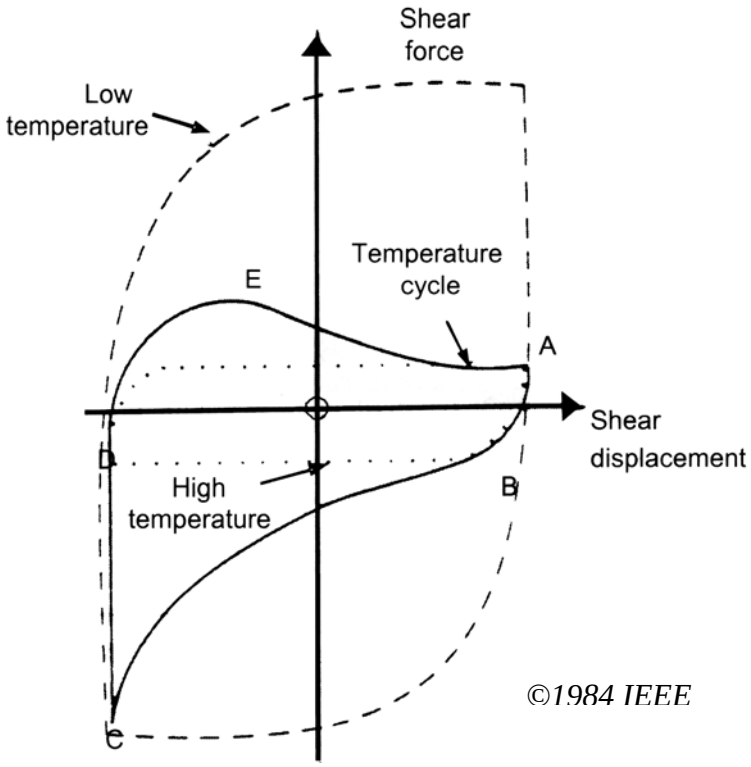

Figure 4: *Stress–strain hysteresis loop of solder interconnections under isothermal cyclic loading and at thermal cycling (reprinted from ref. 69 with kind permission from IEEE).*

The cyclic stress–strain relationship under isothermal (low temperature) cyclic loading constitutes the familiar symmetric hysteresis loop (see Fig. 4). The area contained within the hysteresis loop represents the plastic work done on the material, the width of the loop represents plastic strain range, and the elastic strain range is given by the difference between the total strain and the plastic strain. However, the strength of solder interconnections decreases with increasing temperature. Thus, more extensive deformation takes place in the high temperature part of the cycle and deformation is

much less pronounced in the lower temperature part. The result is a highly asymmetric hysteresis loop where the maximum stress values at high temperatures are appreciably smaller than those at low temperatures.

Experimental measurements have shown that the near eutectic SnAgCu alloys have higher yield strength and higher ultimate tensile strength than eutectic SnPb, even when tested at the same homologous temperature [70-72]. This has been attributed to the more uniform distribution of eutectic phases and the larger volume fraction of intermetallic compounds in the near eutectic SnAgCu alloys [71]. Owing to the higher strength of the near eutectic SnAgCu alloys, however, they are less ductile than the eutectic SnPb. Deformation of the solder interconnections during low cycle fatigue is largely plastic, on the other hand, and endurance of the interconnections is determined principally by ductility rather that strength [73]. The softer the solder material, the more plastic is the deformation and thus, the interconnections are more susceptible to fatigue, which will ultimately reduce the reliability under low cycle thermomechanical loading.

Standardized thermal cycling tests extend the typical operation temperature interval experienced by portable devices during their use in order to accelerate the occurrence of failures. The IEC standard 68-2-14, which was utilized in the experimental part of this work, places the extreme temperatures to - 45 °C and + 125 °C with 15 minutes dwell time at each temperature [74]. For the eutectic Sn3.4Ag0.8Cu [75,77] alloy this temperature interval is equal to 0.5 – 0.8 in terms of homologous temperature, which means that creep processes will contribute to plastic deformation during thermal cycling. The inclusion of a dwell period thus enables more excessive plastic deformation. Since the strength of solder interconnections increases with diminishing temperature, and creep processes are much slower at low temperatures, plastic deformation is less extensive on strain reversal to low temperatures.

Because plastic deformation taking place during thermomechanical loading causes evolution of interconnection microstructures, investigations of the failure mechanism should start from the as–solidified microstructure. At the beginning of solidification, primary grains are formed and their morphology affects the final microstructure. In near–eutectic SnAgCu solders, the primary crystals may be β–Sn, Cu_6Sn_5, or Ag_3Sn depending on the composition. However, since all the near–eutectic

SnAgCu alloys are exceptionally rich in tin their solidification structures are dictated by the solidification of tin. As shown in Figure 5, the microstructures of near–eutectic SnAgCu solder interconnections are composed of relatively few, typically from two to five, large tin colonies, which are distinguished by high–angle boundaries (orientation difference between adjacent grains greater than 15º). A uniformly oriented cellular solidification structure of tin is enclosed within the colony boundaries and uniformly distributed Cu_6Sn_5 and Ag_3Sn particles surround the Sn cells. When stress is applied to the as–solidified interconnections, a great amount of energy would be required to crack the interconnections by ductile fracture. Therefore, instead of cracking in ductile manner, they undergo microstructural evolution before crack nucleation.

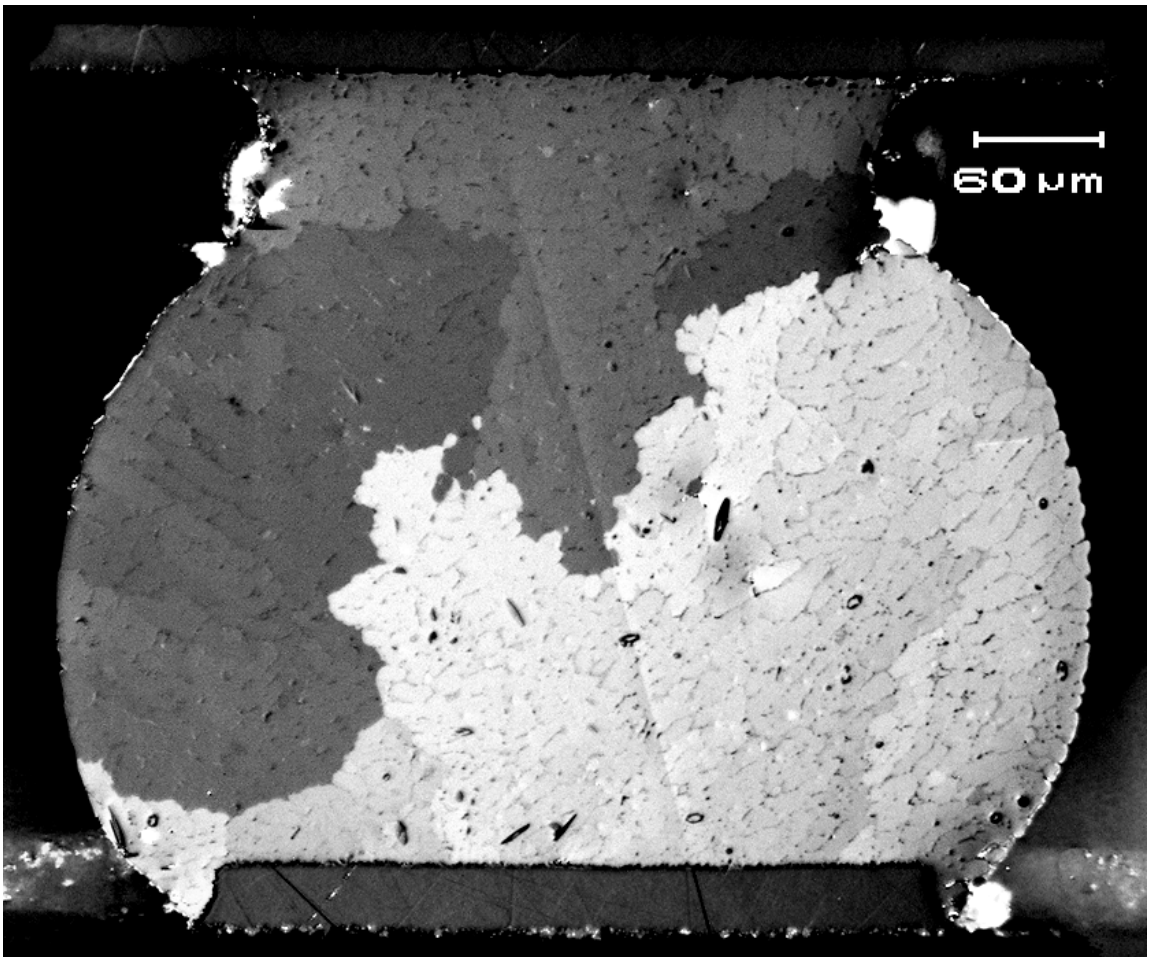

Figure 5: *Optical micrograph obtained with polarized light from a cross–section of the SnAgCu interconnection showing high–angle boundaries between tin grains.*

It has been observed that typically only a fraction of the solder interconnection cross–section actually participates in cyclic deformation because stress distribution inside solder interconnections is seldom uniform. Deformation of the most highly stressed areas of interconnections leads to localized deformation. The recrystallization takes place first in the regions where the microstructure is most heavily deformed plastically and then gradually expands. The thermal anisotropy of the recrystallized grains enhances the nucleation of microcracks along their boundaries (for Sn single crystal at 20°C $\alpha_{[100]} = \alpha_{[010]} = 30.5\text{x}10^{-6}$/°C where as $\alpha_{[001]} = 15.45\text{x}10^{-6}$m/°C [36]). The microcracks coalescence into macroscopic cracks, which eventually propagate through the entire interconnection.

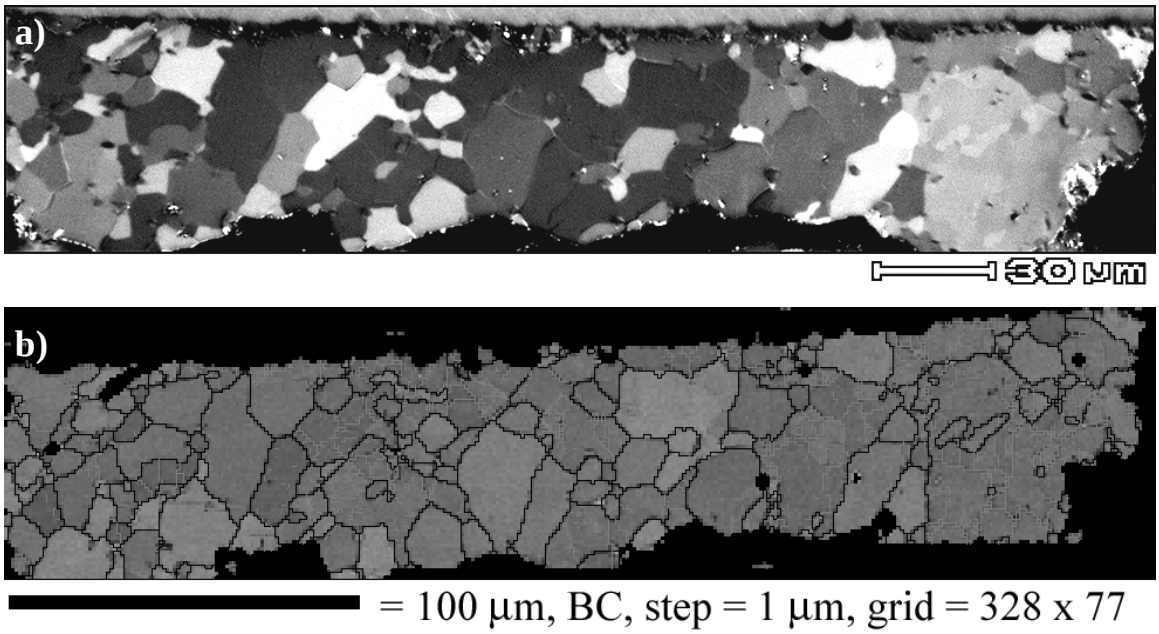

Figure 6: *a) Optical micrograph showing the recrystallized structure on component side interfacial region of the SnAgCu solder interconnection taken with polarized light.*
b) EBSD graph of the same location as in a) showing boundaries with large misorientation (larger than 30°) between the adjacent grains with black lines.

Figure 6(a) shows a micrograph of the recrystallized microstructure on the component side neck region of a thermally cycled interconnection taken with optical microscopy utilizing polarized light. Figure 6(b) shows an Electron Backscatter Diffraction (EBSD) orientation map of the same surface. The EBSD method is explained

in more detail elsewhere [78]. The black lines in Fig. 6(b), which represent the boundaries where the crystal orientation of the adjacent grains exceeds 30°, correspond well with the grain boundaries visible in the optical micrograph in Fig. 6(a). Figure 7 shows how Cu_6Sn_5 and Ag_3Sn intermetallic particles have been left at the grain boundaries as the recrystallized grains of Sn have nucleated and grown. Thus the failure mechanism under thermomechanical fatigue involves the formation of a continuous network of grain boundaries by recrystallization, which enables cracks to nucleate and propagate intergranularly through the solder interconnections.

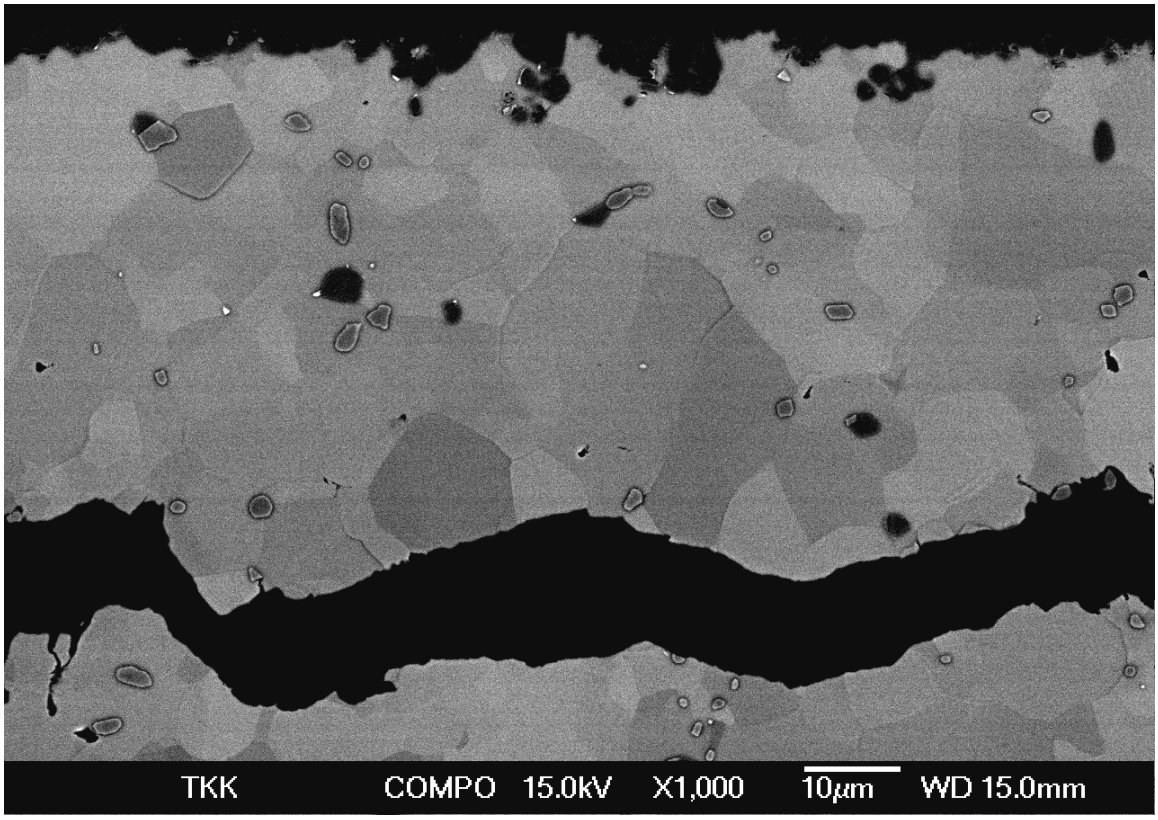

Figure 7: *A backscatter electron SEM micrograph showing small Cu_6Sn_5 and Ag_3Sn particles at grain boundaries between large recrystallized Sn grains.*

3.2 SnAgCu Interconnections Under Mechanical Shock Loading

Several studies carried out with commercial portable electronic products have shown that impact forces generated when products are dropped onto the ground are transmitted through the product casing to the component boards and make the boards

bend and vibrate excessively. The results from product–level tests have been used to develop board–level drop tests [79,80]. JEDEC recently published the JESD22-B111 board–level drop test standard for handheld electronic products. Condition B of the standard was used in the experimental part of this work. Condition B defines the deacceleration pulse as having a shape of half–sine with 0.5 ms width and maximum at 1500 Gs. The shape of the pulse is not only a function of the drop height but depends on the characteristics of the strike surface: drop height determines the maximum deacceleration and strike surface the pulse width. The component board is attached to a support fixture from its four corners with the components facing downwards. The fixture is mounted on a sledge that is dropped down to a rigid surface from a specified height in a controlled manner with the help of two guiding rails. Placing the printed wiring board horizontally results in maximum flexure of the test board. Bending causes displacement between the printed wiring board and the components. Stresses concentrate at the interconnection regions where they cause component, solder interconnection, or board failures. The testing is accelerated because the test structure lacks the support provided by product casings and other adjacent structures.

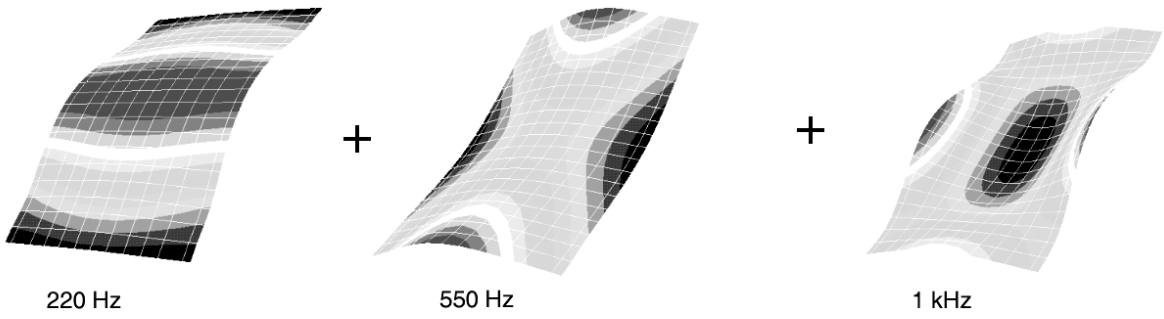

Figure 8: *Total flexure of the test board is the sum of the different natural modes. Three of the most significant natural modes of the JESD22-B111 compliant test board. Different shades of gray represent vertical displacement [76].*

Since the component board is allowed to bend freely at the shock impact, there are numerous different modes in which it can bend. The natural mode of the component board describes the shape where the board bends, and the natural frequency describes how fast the bending takes place. Figure 8 shows three of the most significant natural

modes of the JESD22-B111 compliant test board and their associated natural frequencies. Each of these natural modes vibrates at a characteristic frequency, and the total bending and frequency of the component board is their sum since the different natural modes act simultaneously. The shapes of the natural modes depend on the support structure of the component board, whereas the natural frequencies depend on the stiffness and mass of the component board. The natural modes with highest frequency are usually not of great importance because their amplitude is relatively small and vibrations are attenuated quickly. Only the lowest frequencies, in the case of the JESD22-B111 board the lowest three, are considered significant. Owing to the simultaneous action of many different natural modes and frequencies, and the fast attenuation of the vibration amplitude, the strain distribution on the test board changes very rapidly. Thus, the location of the highest stress changes quickly too. Figure 9 shows the longitudinal strain measured in the middle of the board layout on the opposite side of the board from the components. Figure 9(a) shows how the strain develops after the drop impact. The macroscopic oscillation is due to the natural mode with the lowest frequency. Oscillations at higher frequencies are embedded in the larger strains. The strains due to natural modes with higher frequencies are shown in Fig. 9(b), which presents only the 0 - 5 ms time interval from Fig. 9(a).

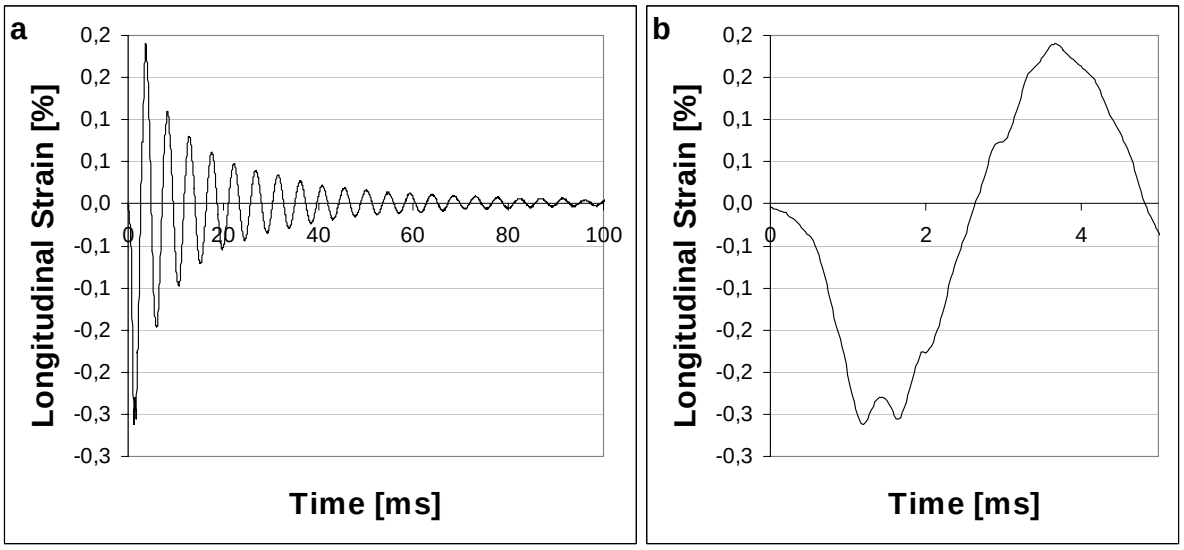

Figure 9: *Measured longitudinal strain at the center of the board [76].*

The failure mechanism under mechanical shock loading differs greatly from that under thermomechanical loading, where the localized recrystallization of the interconnections enables the nucleation and propagation of cracks in the bulk solder. Besides temperature the most important difference between drop tests and thermal cycling tests is the deformation rate. As noted above, at homologous temperatures above 0.3 – 0.4 the deformation of solder interconnections becomes time dependent and the plastic flow depends on the rate of strain. In thermal cycling tests the deformation rate of solder interconnections is in the range of 10^{-4} – 10^{-2} % / s, while in drop tests it is about 1000% / s. Both the ultimate tensile strength and the yield strength increase with strain rate, but the yield stress is typically more strain–rate sensitive [43]. Figure 10 shows the ultimate tensile strength of Sn and two common Sn–based solders, Sn1.5Bi and Sn3.4Ag0.8Cu, as a function of strain rate. As can be seen, when the strain rate is increased from that occurring in thermal cycling to that occurring in drop tests, the flow stress of solder is about two to three times as high.

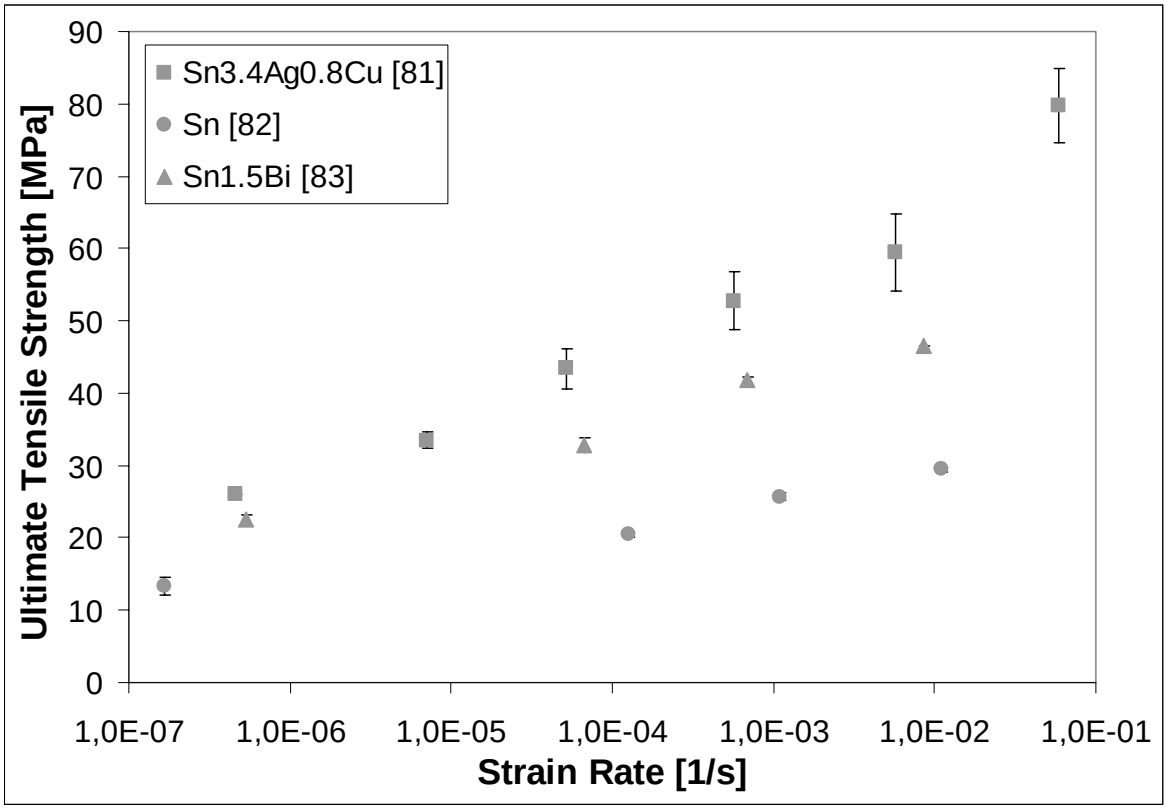

Figure 10: *Effect of strain rate on strength of Sn and two Sn–based solders [81,82,83]*

High deformation rate increases the strength of the solder interconnections, and thereby stresses, especially in interfacial regions where stresses exceed the fracture strength of the brittle intermetallic layers. The bulk solder does not markedly deform plastically, and therefore no recrystallization has been observed after drop testing. As the strain rate is increased, the twinning mechanism can become active. Twins are typically observed in regions of the interconnections where stresses are highest Thus, the strain–rate hardening of the solder interconnections at high deformation rates forces cracks to propagate in the intermetallic compound layers instead of the bulk solder.

4. STATISTICAL METHODS IN RELIABILITY ANALYSIS

Experimental reliability test plans are typically constructed with many variables so that the reliabilities of different combinations of the variables can be compared. Experimental design and statistical significance testing provide a powerful set of tools for carrying out these tests. Significance tests such as the Analysis of Variance and the Wilcoxon Rank–Sum test can be utilized to study the differences in reliability. The Weibull reliability analysis supplements the statistical analysis by incorporating the classification of failure modes into a numerical reliability analysis. It has also become common practice to report the different Weibull parameters of reliability tests. The impact of different factors is sometimes studied with one factor at a time experiments. The drawback of this approach is that when factors are studied independently, misleading conclusions may be drawn because the possible interaction between the factors is neglected. Factorial experiments combined with statistical analysis have been developed to overcome this problem. A factorial experiment allows the researcher to study the main effects of each factor as well as their interactions, and statistically determine their significance.

4.1 Factorial Experimental Designs and Significance Testing

There are two important principles in the statistical testing of factorial experiments: replication and randomization [84]. By repeating (i.e. *replicating*) experiments, an estimate is obtained of the experimental error. The inference of the significance is based on the experimental error. To eliminate any systematic error from the test data, the order of the experiments is independently *randomized*. In the following, experimental designs and significance testing are discussed starting with the single–factor experiments, and then moving on to experiments with more factors and their interactions taken into consideration.

4.1.1 Single–Factor Experiments

Experiments with a single factor are called 'one–way classification fixed–effect experiments'. The term '*one–way classification'* means that the purpose of the experiment is to study the impact of only one factor on the response. The factor studied should have at least two different levels. The term '*fixed effect'* means that levels of the factor are not random but assigned by the experimenter.

The choice of statistical method for significance testing depends on how well the test data conforms to normal distribution. If the reliability data is normally distributed the results from the experiment can be analyzed with a parametric method such as the Analysis of Variance (ANOVA). If the data fails to conform to the normal distribution, a nonparametric method such as the Wilcoxon Rank–Sum Test must be used instead. The conformance of the data to the normal distribution is studied by one of the many goodness–of–fit tests: the Anderson–Darling Test, the Shapiro–Wilk Test, or the Kolmogorov–Smirnov Test, for instance [85]. A probability value for rejecting the null hypothesis is obtained from a statistical computer program or is read from the probability table of the tests. Tests are typically carried out at less that 5% risk level, which means that if the resulting p–value of the test is below 5% there is a good reason to reject the null hypothesis and conclude that the distribution conforms to the normal distribution.

The analysis of variance tests the difference between the mean values of two samples by testing the following hypotheses: H_0: $\sigma^2_1 = \sigma^2_2 = ... = \sigma^2_k$; H_1: $\sigma^2_i \neq \sigma^2_j$, where σ^2 denotes the unknown true variance. The basic principle of the ANOVA is that the total variation (SS_{Tot}) in the response can be subdivided into components that can be attributed to recognizable sources of variation. Some of the variability can be explained by the different factor levels that are used and the rest is due to random fluctuation within the same factor level. The variation is quantified by the sum of squares identity, which can be written as $SS_{Tot} = SS_{Levels} + SS_{Err}$. If there is a significant difference in the means, most of the variation in the response is due to the different levels of the factor, i.e. to SS_{Levels}. The ANOVA procedure uses this idea of comparing the significance of the difference between the SS_{Levels} and SS_{Err} by an appropriate F–ratio to test the null hypothesis of equal treatment means [85]. If H_0 is true, the F–ratio is expected to be close to 1. The p–value is typically obtained by statistical softwares or it can be read from the F–distribution table. The p–value is the risk level at which the rejection of the null hypothesis is made. A p-value below 5% can be taken as a good indication to reject the null hypothesis and conclude that the two means are significantly different. The results are typically presented in the ANOVA table.

The Wilcoxon rank–sum test is a method for hypothesis testing when the assumption of normality is not met [86]. The hypotheses are stated in terms of equal population medians: H_0: $M_1 = M_2$; H_1: $M_1 \neq M_2$. The test is based solely on the order in which the observations from the two samples fall: the two observations are pooled (group identities retained), ordered from smallest to largest, and ranked. The sum of the ranks associated with the samples is calculated and p–values for rejecting the null hypothesis is read from a probability table.

4.1.2 Factorial Designs

Experiments for investigating the effects of two or more factors at a time are called *factorial experiments*. Different designs are denoted a^k factorial designs, where a represents the number of levels and k the number of factors. A factorial experiment where all the different combinations of factor levels are tested is called a *full–factorial*

experiment. A change in the response caused by a change in the level of a factor is called a *main effect*. If the difference in the responses between the levels of one factor is not the same at all levels of the other factors, there is an interaction between the factors and this is called an *interaction effect*.

Figure 11 shows a 2^2 experimental design. The main effect for factor A is the average difference in the response between the two levels chosen [84]. A positive value means that increasing the factor from the lower level to the upper level causes an increase in the response. If the sign of the main effects of both factors is the same, either positive or negative, no interaction exists and the interaction term is close to zero. When the interaction effect is nonzero, interaction exists between the two factors. The significance of the increase or decrease in the response is tested statistically.

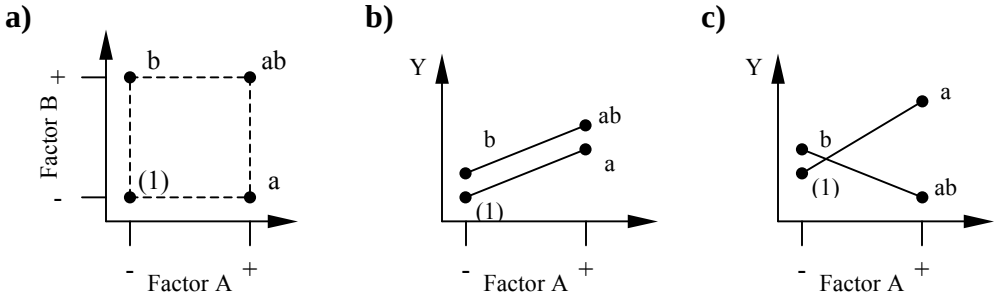

Figure 11: a) *Factorial design, b) no interaction, c) interaction*

The 2^2 factorial design can be generalized to 2^k factorial designs to take more factors into account. The graphical presentation becomes complicated, however (see Fig. 12) and experimental design matrixes are used instead [84].

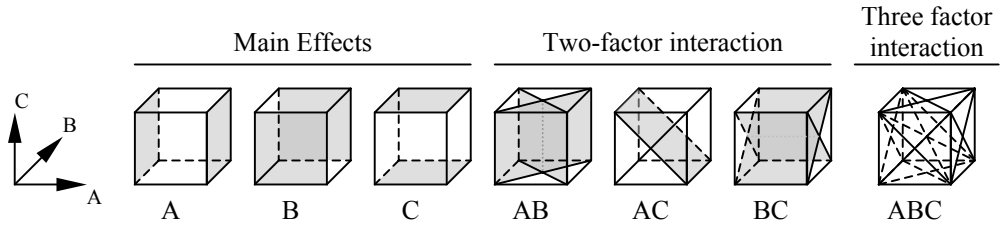

Figure 12: *Graphical presentation of contrasts corresponding to the main effects and interactions in the 2^3 design*

The ANOVA of the results from two or more factor experiments follows the same principles as the one–way ANOVA. The total variation (SS_{Tot}) is again subdivided into components that can be attributed to recognizable sources of variation ($SS_{Factors}$ and SS_E). However, this time several factors as well as their interaction are present. In the case of a two–factor experiment, this means that the $SS_{Factors}$ breaks down into three different components: effects due to factors A and B and to their interaction AB. The variation can be quantified by the sum of squares identity: $S_{Tot} = SS_A + SS_B + SS_{AB} + SS_E$. The two–way classification can also be expressed as $Y_{ijk} = \mu + \alpha_i + \beta_j + (\alpha\beta)_{ij} + E_{ijk}$, where i=1,2,…,a and j=1,2,…,b are the number of levels. This presentation shows symbolically how each observation can be partitioned into five components. The μ represents the true mean of the quality characteristic. α_i and β_j are the effects of factors A and B on the mean value of the quality characteristic, while $(\alpha\beta)_{ij}$ is the effect of the interaction. (Note that $\alpha\beta$ does not stand for α times β.) E_{ijk} is the random dispersion due to unexplained sources of variation. This notation shows how the different factors $(\alpha_i + \beta_j + (\alpha\beta)_{ij} + E_{ijk})$ affect the true mean μ of the characteristic, which can be seen in the response measure. This model is important since it is used to state hypothesis about the effects of different factors.

The first hypothesis to be tested is the null hypothesis of interaction: H_0: $(\alpha\beta)_{ij}=0$. If the null hypothesis is rejected, it implies that both the main effects are significant. If it is not rejected, the analysis is carried out further by testing the null hypothesis of no difference between the levels of factors A and B: H_0^I: $\alpha_1=\alpha_2=\ldots=\alpha_a=0$ and H_0^{II}: $\beta_1=\beta_2=\ldots=\beta_b=0$, respectively. Testing the null hypothesis is again carried out with the F–ratio. The appropriate F–ratio is developed in the same manner as discussed above in connection with the single–factor experiments. If H_0 is not true, the F–ratio is close to 1 and the p–value is small, less than 5%. Table I presents the complete ANOVA table for two-way classification with fixed effects.

Table I: *The ANOVA table for the two–way classification design with fixed effects.*

Source of Variation	Degrees of Freedom	Sum of Squares	Mean Squares	F	P
A	$a-1$	SS_A	$\frac{SS_A}{a-1}$	$\frac{MS_A}{MS_E}$	p_A
B	$b-1$	SS_B	$\frac{SS_B}{b-1}$	$\frac{MS_B}{MS_E}$	p_B
AB	$ab-1$	SS_{AB}	$\frac{SS_{AB}}{(a-1)(b-1)}$	$\frac{MS_{AB}}{MS_E}$	p_{AB}
Error	$ab(n-1)$	Subtraction	$\frac{SS_E}{ab(n-1)}$		
Total	$abn-1$	SS_{Tot}			

If the null hypothesis is rejected, it is concluded that the factor has a significant impact on the response. However, what the analysis does not say is what level of the factor yields the desirable value. In other words, rejecting H_0^I: $\alpha_1=\alpha_2=\ldots=\alpha_a=0$ implies that one or more of the equalities does not hold and therefore at least two of the population means are different. There are several techniques to make these distinctions: the Bonferroni T–test and the Duncan's multiple range tests, for instance. The Bonferroni procedure compares population means via the T–test. However, the method is only feasible when the number of population means (factor levels) is fairly small. This is because as the number of population means increases, the overall probability of error may become unacceptably high, resulting in a test with little power. The Duncan's multiple range test calculates the difference between the largest and smallest sample means and if this is found to be significant, the range is reduced until no statistically significant differences are found.

If the reliability data fails to conform to the normal distribution, the statistical testing must be carried out by individually testing all the pair–wise differences. The 2^2 factorial design presented in Figure 11 can be analyzed rather easily with the Wilcoxon rank–sum test, but designs with more than two factors become very complicated to analyze.

4.2 Weibull Reliability Analysis

The Weibull probability density function and cumulative density function as well as their associated parameters and their estimation are now discussed.

4.2.1 The Weibull Distribution

Reliability is the ability of a product to operate without failure under a set of predetermined conditions over a specified period of time [87]. This ability is expressed in terms of probability, which can be described by a distribution. The Swedish statistician Waloddi Weibull published his distribution for the first time in 1939 [88] but it did not attract international attention until 1951 [89]. Even though he developed a distribution function for the ultimate tensile strength of materials his approach was purely mathematical. He supposed that the strength distribution of a material could be specified by a function including two or three parameters. Later on in 1951 he published the hallmark paper, where he showed with seven examples from widely different fields that his distribution could be applied to a variety of different applications. The Weibull distribution is a widely used lifetime distributions in reliability engineering and life data analysis due to its versatility. Depending on the values of the parameters, it can be made to fit many life distributions. Furthermore, it can be used with relatively small sample sizes and then underlying failure modes and mechanisms can be classified with the help of the β-parameter. The Weibull probability density function and the cumulative distribution function are given by

$$f(t) = \left(\frac{\beta}{\eta-\gamma}\right)\left(\frac{t-\gamma}{\eta-\gamma}\right)^{\beta-1} \exp\left[-\left(\frac{t-\gamma}{\eta-\gamma}\right)^{\beta}\right] \text{ and}$$

$$F(t) = 1 - \exp\left[-\left(\frac{t-\gamma}{\eta-\gamma}\right)^{\beta}\right],$$

respectively, where η is the characteristic life, β is the shape parameter, and γ is the location parameter [90].

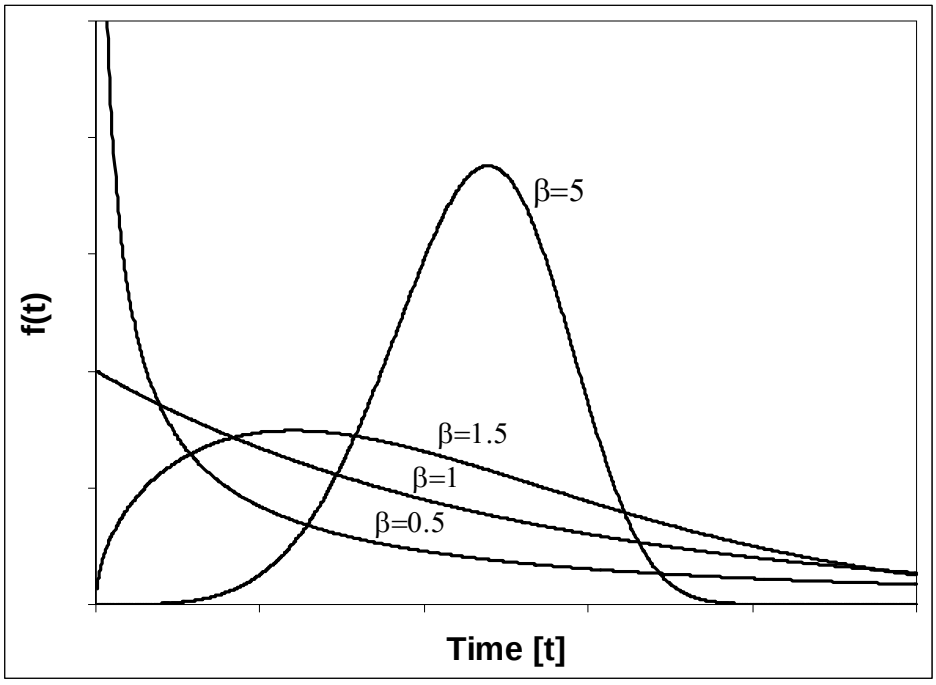

Figure 13: *Weibull probability density functions with different values of β*

A change in the scale parameter η has the same effect on the distribution as a change of the time scale; when η is increased while keeping β constant, the probability density function stretches out and decreases in height because the area under the density function is a constant value of one. The characteristic life is related to the mean time–to–failure by $\mu=\eta\Gamma(1+1/\beta)$. The location parameter γ is very often zero, and we speak of the two–parameter Weibull distribution. However, the three–parameter Weibull distribution can be utilized to better fit the function to the data. A change in gamma slides the distribution along the time axis without affecting the shape of the distribution. When γ is greater that zero, the distribution starts at the location depicted by the value of γ. Gamma may have positive or negative values. However, a negative value indicates unrecorded lifetime before the start of the test, during which failures have occurred. With different β parameters, the function takes a variety of shapes as shown in Figure 13. The Weibull function can also be used to approximate several other distributions: when β = 1 it is

identical with the exponential distribution, and when β = 2 it is identical with the Rayleigh distribution. When β = 2.5 it approximates the lognormal distribution, and when β = 3.5 it approximates the normal distribution [91]. Beta is related to the variance by $\sigma^2=\eta^2[\Gamma(1+2/\beta)-\Gamma^2(1+1/\beta)]$.

Even though the Weibull distribution function does not have a physical basis [88,89], there is an important feature regarding the interpretation of the β–parameter, which implies, in part, why the Weibull analysis has gained such popularity in the field of electronics reliability: The feature is that the failure rate (λ) has a distinct effect on the value of β. The failure rate is given by

$$\lambda(t)=\frac{f(t)}{1-F(t)}=\left(\frac{\beta}{\eta-\gamma}\right)\left(\frac{t-\gamma}{\eta-\gamma}\right)^{\beta-1}.$$

The value of β = 1 divides the behavior of the Weibull function: values of β < 1 correspond to decreasing failure rate, β = 1 to constant failure rate, and β > 1 to increasing failure rate. Figure 14 shows this graphically.

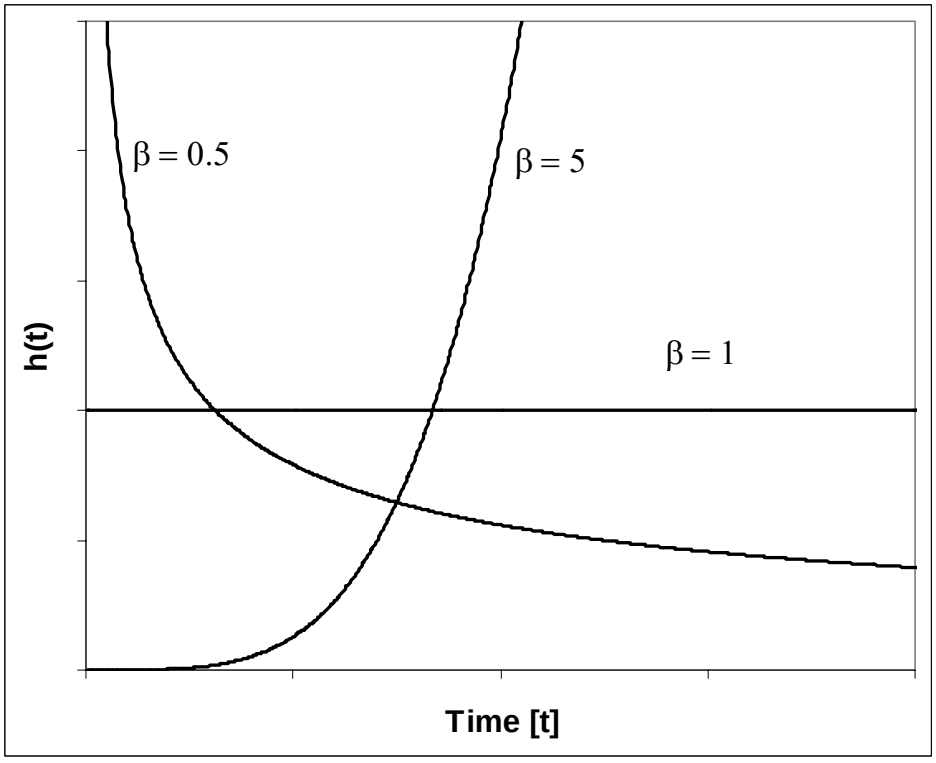

Figure 14: *The Weibull failure rate with different values of β*

The curves in Figure 14 comprise the three sections of the classic bathtub curve (see Fig. 15). All three life–stages of the bathtub curve can thus be mathematically represented with the Weibull distribution by means of the parameter β. When the β value is less than unity the plot represents "infant mortality" failures [decreasing λ(t)], when β equals one the plot represents the failures during the "useful lifetime" [constant λ (t)], and when β is greater than one the distribution represents the "wear–out" failures [increasing λ (t)].

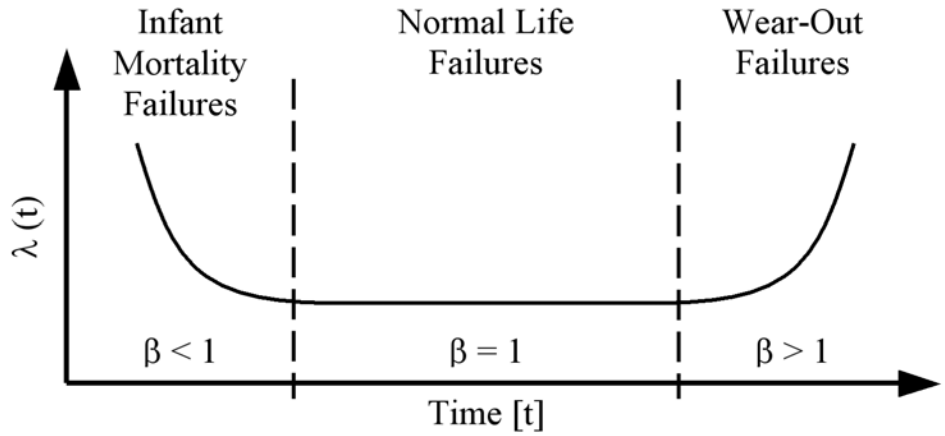

Figure 15: *Relationship between the Weibull shape parameter β and the bathtub curve.*

Thus, failures can be classified into three categories on the basis of the obtained β–parameter; however, the failure mechanism associated with the β parameter has to be determined by physical failure analysis. Ideally, each value of beta depicts a single failure mode, but there may also be several failure modes acting simultaneously, and many different mechanisms may be confounded in the beta value. Thus, each failure mode needs to be identified and a separate analysis carried out for each.

4.2.2 Estimation of the Weibull Parameters

Many methods are available for the Weibull parameter estimation, for example, probability paper plotting, maximum likelihood estimation, and the method of least

squares regression. Probability paper plotting involves subjectivity at the visual fit of the regression line, and in this work the method of least squares was preferred. The method of least squares is a mathematical version of probability plotting and brings objectivity to the parameter estimation. It is chosen instead of the maximum likelihood estimation because of its relative simplicity. Furthermore, maximum likelihood is asymptotically efficient, i.e. it produces the most precise estimations for large sample sizes, from fifty to one hundred and above [85]. With fewer samples it can be seriously biased.

The parameters are estimated from a given dataset in the following manner: By taking double logarithms and making the necessary transformations, the cumulative distribution function takes the form

$$\log_{10} \ln\left(\frac{1}{1-F(t)}\right) = \beta \log_{10}(t) - \beta \log_{10}(\eta)$$

which is a linear function of log(t) with slope equal to β and the y–axis interception equal to -βlog(η). The times–to–failure are first rearranged in increasing order and y = logln[1/{1-F(t)}] is cumulatively plotted against x = log(t).

The mean rank method is an appropriate method to estimate the cumulative distribution function F(t) when the distribution is symmetrical [91]. However, this is seldom the case and F(t) is more commonly estimated by the median rank. It can easily be estimated using the following approximation, where *i* is the order of the value and *n* is the sample size:

$$\hat{F}(t) = \frac{i - 0.3}{n + 0.4}.$$

The next step is to fit a straight line to the scatter plot using ***least–squares regression***. The best fit of the linear function $y = b_0 + b_1 x$ is achieved by choosing b_0 and b_1 so that the distances from individual data points to the regression line are minimized. This is done through minimizing the sum of the distances squared. If the data points fit well to the linear assumption, the parameters can be adequately estimated using the two–parameter distribution. If the fit is insufficient, the two–parameter distribution may not

give the most accurate results and the presence of failure–free time (γ) or mixed failure modes should be considered. A slightly concave behavior in the region of lower failure probability indicate the presence of a failure–free life whereas sharp corners may indicate a mixture of failure modes. The only way to determine which is responsible for the poor fit is to use physical failure analysis to determine the number of failure modes. A separate Weibull plot is made for each failure mode, and if the classification is correct the plots will show good fit. The fit of the distribution can be evaluated with the aid of correlation coefficient but the cumulative nature of the plot increases the observed correlation and therefore goodness-of-fit tests should be used to confirm that experimental data is distributed according to the selected distribution. There are alternative methods to do the testing such as the chi-square test and the Kolmogorov-Smirnov test [85]. Many commercial softwares have specialized procedures that combine information from different test. The slope of the regression line provides an estimate of β. The y–intercept of the regression line can be used to estimate the characteristic lifetime: $\eta = 10^{-\frac{y_0}{\beta}}$. The η value can also be read from the diagram at the 63.2% cumulative failure rate of the regression line.

5. SUMMARY OF THE THESIS

The two different loading types, namely thermomechanical and mechanical shock loadings, and their effects on strains and stresses experienced by solder interconnections were discussed in the introductory section of the thesis. In thermal cycling tests the reliability of SnAgCu solder interconnections was found to be dependent on their recrystallization characteristics and therefore deformation and restoration of solder interconnections were discussed in detail. Different fracture mechanisms of Sn-based solder interconnections were also reviewed. Because the loading rate is perhaps the most important difference between the two reliability tests, the effect of different strain rates on the properties of solder interconnections was also discussed. Finally, the statistical methods applied in the thesis were introduced.

The objective of this work was to obtain better understanding of the failure mechanisms affecting portable electronic products in typical use environments. The reliability was studied by employing standardized thermal cycling and drop tests because portable electronic products are exposed during typical operation to temperature fluctuations, caused by internally generated heat dissipation or by external environment, and to mechanical shock loads, caused by dropping. The lead–free materials used in the reliability tests were chosen to represent those typically used in portable electronic products, and the test boards were assembled on a full–scale production line, as in volume production. Ni(P)|Au or organic soldering preservative (OSP) protective coatings were used on the printed wiring boards (PWB), and Ni|Au or bare Cu were used as the under bump metallization (UBM) on the component side. Components were reflow soldered with different commercial near–eutectic SnAgCu solder pastes, but the effect of the pastes on the nominal composition of the interconnections was found to be insignificant. It is the solder bump material that mostly determines the composition of the solder interconnections after the reflow.

A microstructural approach was combined with a statistical analysis of the reliability test data. Statistically significant differences were found between the times–to–failure of the different PWB protective coatings and under bump metallizations. The failure mechanism under thermomechanical loading is determined by the kinetics of recrystallization, which in turn is strongly influenced by the microstructures formed during soldering. Component metallizations and PWB protective coatings affect the microstructures by dissolving into the molten solder during soldering. The dissolution rate of Cu into the melt was considerably higher than that of Ni and the solidification of the liquid interconnections led, therefore, to different microstructures. The microstructure of the interconnections on the Cu|OSP–coated soldering pads was more heterogeneous than that of the interconnections on the Ni(P)|Au due to the presence of numerous primary Cu_6Sn_5 particles. The large primary Cu_6Sn_5 particles enhance the onset of recrystallization and therefore cracking of the interconnections on the Cu|OSP, under thermomechanical loading, takes place faster. Under mechanical shock loading, in contrast, the reliability of solder interconnections is determined by the properties of the intermetallic compound layers because the strain–rate hardening of the solder material

forces cracks to propagate in these brittle layers instead of the bulk solder. Under mechanical shock loading the reliability of interconnections on the Ni(P)|Au is inferior to that of interconnections on the Cu|OSP due to the formation of complex P–rich reaction layers between the Ni(P) coating and the solder. Cracks nucleate and propagate in the porous and highly brittle NiSnP layer between the columnar two–phase (Ni_3P +Sn) layer and the $(Cu,Ni)_6Sn_5$ intermetallic layer. Interconnections on Cu|OSP PWB protective coatings, in turn, fail by cracking of the intermetallic compound layers on the component side. The binary Cu_6Sn_5 formed on bare Cu UBM shows good structural integrity under mechanical shock loading conditions, while the $(Cu,Ni)_6Sn_5$ formed on the Ni UBM is weaker.

Because portable electronic products are seldom dropped soon after they are assembled, the effects of strains and stresses during normal operation were simulated with thermal cycling or isothermal annealing treatment before the drop testing. When thermal cycling preceded the drop test the failure mode changed to intergranular fracture through the bulk solder, and the failure mode was the same regardless of the PWB coating and the UBM. The high-angle boundaries between the recrystallized grains generated during thermal cycles provide paths along which cracks can propagate. The drop test reliability performance can improve due to the thermal cycles experienced before drop testing because more impacts are required for the cracks to propagate through the bulk solder than through the brittle intermetallic layers. On the other hand, prolonged lifetime at elevated temperatures can reduce the drop test reliability considerably due to the formation of Kirkendall voids in the Cu_3Sn intermetallic layers.

The thesis includes five publications, the main results of which are summarized in the following.

Publication I, entitled "Impact of printed wiring board coatings on the reliability of lead–free chip–scale package interconnections", describes an investigation of the failure mechanism of CSP interconnections under thermomechanical loading (IEC 68-2-14N). The microstructure of the as–soldered near–eutectic SnAgCu solder interconnections was characterized by only a few large grains. Under the cyclic loading, cracking of the solder interconnections takes place only after recrystallization has created

networks of grain boundaries along which the cracks can propagate intergranularly. The reliability of interconnections on two different PWB protective coatings was compared. Interconnections on Ni(P)|Au were more reliable than those on Cu|OSP ($\alpha < 5$ %), and the difference was explained in terms of observed differences in the microstructures. The primary Cu_6Sn_5 particles dispersed in the solder matrix of the Cu|OSP interconnections decrease the incubation time for the recrystallization by providing favorable nucleation sites for the recrystallizing grains. Because the interconnections on Cu|OSP recrystallize faster, cracks can nucleate earlier, and the interconnections fail before those on Ni(P)|Au.

Publication II, entitled "Reliability of CSP interconnections under mechanical shock loading conditions", presents all the different failure modes in assemblies subjected to drop test conditions (JESD22-B111). The test boards differed in type of surface finish (Ni(P)|Au or Cu|OSP) and pad structure (via–in–pads or no vias). The components soldered on Cu|OSP were more reliable than those soldered on Ni(P)|Au, and the no via–in–pad structure was more reliable than the via–in–pad structure ($\alpha < 5\%$). The loading of the boards was examined by measuring strains at different locations. From the measured strains, stresses in the solder interconnections were calculated with the FEM. The reasons for the differences in the failure modes under thermomecahnical cycling and mechanical shock loading were considered and an explanation for the differences in the failure mechanisms was proposed: under high deformation rates, the strain–rate hardening of the solder material forces cracks to propagate in the intermetallic compound layers rather than the bulk solder, whereas under thermomechanical loading the localized recrystallization of solder controls the nucleation and propagation of cracks in the bulk solder.

Publication III, entitled "Failure mechanisms of lead–free chip scale package interconnections under fast mechanical loading", investigates the observed reliability difference between the components soldered on Cu|OSP and the components soldered on Ni(P)|Au. In the case of the Cu|OSP, cracks propagate in the $(Cu,Ni)_6Sn_5$ reaction layer on the component side because the strain–rate hardening of the solder interconnections rapidly increases the stresses in the corner regions of the interconnections above the fracture strength of the intermetallic layer, leading to intermetallic fracture. In interconnections on the Ni(P)|Au, cracks nucleate and propagate in the porous NiSnP

layer between the columnar two–phase (Ni_3P +Sn) layer and the $(Cu,Ni)_6Sn_5$ intermetallic layer. The Ni(P)|Au interconnections fail at the PWB side even though higher stresses are generated on the component side because of the highly brittle nature of the reaction layer.

In the work reported in publication IV, "Reliability of lead–free interconnections under consecutive thermal and mechanical loadings ", thermal cycling (IEC 68-2-14N) or isothermal annealing treatment was carried out before the standard drop test (JEDS22-B111) in order to simulate more realistically the effects of strains and stresses on the reliability of portable electronic products during use. The lifetime in the drop test was increased when thermal cycling was carried out before drop testing as compared with drop test results of the as–soldered assemblies (α = 19%). Recrystallization had formed networks of grain boundaries during thermal cycling, enabling the cracks to propagate intergranularly in the bulk solder as long as there were grain boundaries available. If the crack tip reaches the boundary of a recrystallized area it continues to propagate in the intermetallic compound layers due to the increased flow–stress of the non–recrystallized part of the interconnections. In contrast to as soldered assemblies, the reliability in drop tests decreased dramatically when isothermal annealing was carried out before the drop testing (α < 5 %). The annealing treatment enabled the formation of Kirkendall voids in the Cu_3Sn layer, which constituted almost continuous paths. The cracks nucleate in the bulk solder, but directly after the nucleation they enter the Cu_3Sn layer and propagate through the entire interconnection. The effect of component–side metallization on the drop test reliability was also studied with as–soldered assemblies. The copper was found to be more reliable than the electrochemical nickel (α < 5 %). It seems evident that dissolved Ni lowers the fracture strength of $(Cu,Ni_6)Sn_5$.

Publication V, entitled "Metallurgical factors behind the reliability of high–density lead–free interconnections" describes the formation of microstructures in lead–free solder interconnections at soldering and their evolution during accelerated reliability tests. The focus was on identifying the factors driving the microstructural evolution and the effects of different testing conditions. Reliability of the solder interconnections was examined in the light of two case examples, namely thermal cycling and mechanical

shock loading. The research approaches and some of the methods also utilized in the work were presented.

REFERENCES

1. Directive 2002/96/EC of the European Parliament and of the council on Waste of Electrical and Electronic Equipment (WEEE), Jan. 27th, 2003.
2. Directive 2002/95/EC of the European Parliament and of the council on the Restriction of the use of Hazardous Substances in Electronic and Electronic Equipment (RoHS), Jan. 27th, 2003.
3. Commission decision 2005/618/EC amending directive 2002/95/EC of the European Parliament and of the Council for the purpose of establishing the maximum concentration values for certain hazardous substances in electrical and electronic equipment, Aug. 18th, 2005.
4. C. M. L. Wu, D. Q. Yu, C. M. T. Law, and L. Wang, "Properties of lead–free solder alloys with rare earth element additions", *Materials Science and Engineering R*, **44**, (2004), pp. 1–44.
5. K. N. Tu, A. M. Gusak, and M. Li, "Physical and materials challenges for lead–free solders", *Journal of Applied Physics*, **93**, 3, (2003), pp.1335–1353.
6. W. Peng, K. Zeng, and J. Kivilahti, "A literature review on potential lead–free solder systems", Espoo, Helsinki University of Technology, Report Series HUT–EPT–1, (2000), p. 53.
7. P. T. Vianco and D. R. Frear, "Issues in the replacement of lead–bearing solders", *Journal of Metals*, **7**, (1993), pp. 14–18.
8. C. M. Miller, I. E. Anderson, and J. F. Smith, "A viable tin–lead solder substitute: Sn–Ag–Cu", *Journal of Electronic Materials*, **23**, 7, (1994), pp. 595–602.
9. I. E. Anderson, "Tin–silver–copper: a lead free solder for broad applications", *The Proceedings of the NEPCON West'96*, Anaheim, CA, March 25–28, 1996, IEEE, **2**, (1996), pp. 882–885.

10. E. Bradley and J. Hranisavljevic, "Characterization of the melting and wetting of Sn–Ag–X solders", *IEEE Transactions on Electronics Packaging Manufacturing*, **24,** 4, (2001), pp. 255–260.
11. Y. W. Yen and S. W. Chen, "Phase equilibria of the Ag–Sn–Cu ternary system", *Journal of Materials Research*, **19**, 8, (2004), pp. 2298–2305.
12. K. W. Moon and W. J. Boettinger, "Accurately determining eutectic compositions: the Sn–Ag–Cu ternary eutectic", *Journal of Materials*, **56**, 4, (2004), pp. 22–27.
13. D. Q. Yu, J. Zhao, and L. Wang, "Improvement on the microstructure stability, mechanical and wetting properties of Sn–Ag–Cu lead–free solder with the addition of rare earth elements", *Journal of Alloys and Compounds*, **376**, 1–2, (2004), pp. 170–175.
14. K. S. Kim, S. H. Huh, and K. Suganuma, "Effects of fourth alloying additive on microstructures and tensile properties of Sn–Ag–Cu alloy and joints with Cu", *Microelectronics Reliability*, **43**, 2, (2003), pp. 259–267.
15. D. R. Frear, J. W. Jang, J. K. Lin, and C. Zhang, "A metallurgical study of Pb–free solders for flip–chip interconnects", *Journal of Metals*, **53**, 6, (2001), pp. 28–32.
16. R. Ninomiya, K. Miyake, and J. Matsunaga, "Microstructure and mechanical properties of a new lead–free solder", *The Proceedings of INTERPack '97*, Kohala Coast, HI, June 15–19, 1997, ASME, **2**, (1997), pp. 1329–1333.
17. U. R. Kattner and W. J. Boettinger, "On the Sn–Bi–Ag ternary phase diagram", *Journal of Electronic Materials*, **23**, 7, (1994), pp. 603–610.
18. R. K. Shiue, L. W. Tsay, C. L. Lin, and J. L. Ou, "A study of Sn–Bi–Ag–(In) lead–free solders", *Journal of Materials Science*, **38**, (2003), pp. 1269–1279.
19. Z. Xia, Y. Shi, and Z. Chen, "Evaluation on the characteristics of tin–silver–bismuth solder", *Journal of Materials Engineering and Performance*, **11**, 1, (2002), pp. 107–111.
20. J.–W. Choi and T.–S. Oh, "Shear strength and aging characteristics of Sn–Pb and Sn–Ag–Bi solder bumps", *Advances in Electronic Materials and Packaging*, **11**, (2001), pp. 433–437.

21. J. S. Hwang, "A strong lead–free candidate: the Sn/Ag/Cu/Bi system", *Surface Mount Technology*, **14**, 8, (2000), pp. 20–22.
22. C. Andersson, Z. Lai, J. Liu, H. Jiang, and Y. Yu, "Comparison of isothermal mechanical fatigue properties of lead–free solder joints and bulk solders", *Materials Science and Engineering A*, **394**, 1–2, (2005), pp. 20–27.
23. M. Amagai, M. Watanabe, M. Omiya, K. Kishimoto, and T. Shibuya, "Mechanical characterization of Sn–Ag–based lead–free solders", *Microelectronics Reliability*, **42**, 6, (2002), pp. 951–966.
24. D. Shangguan and A. Achari, "Evaluation of lead–free eutectic Sn–Ag solder for automotive electronics packaging applications", *The Proceedings of the 16th International Electronics Manufacturing Technology Symposium*, La Jolla, CA, Sept. 12–14, 1994, IEEE/CPMT, **1**, (1994), pp. 25–37.
25. M. M. El–Bahay, M. E. El Mossalamy, M. Mahdy, and A. A. Bahgat, "Some mechanical properties of Sn–3.5Ag eutectic alloy at different temperatures", *Journal of Materials Science: Materials in Electronics*, **15**, 8, (2004), pp. 519–526.
26. H. Mavoori, J. Chin, S. Vaynman, B. Moran, L. Keer, and M. Fine, "Creep, stress relaxation and plastic deformation in Sn–Ag and Sn–Zn eutectic solders", *Journal of Electronic Materials*, **26**, 7, (1997), pp. 783–790.
27. S. Choi, J. P. Lucas, K. N. Subramanian, and T. R. Bieler, "Formation and growth of interfacial intermetallic layers in eutectic Sn–Ag solder and its composite solder joints", *Journal of Materials Science: Materials in Electronics*, **11**, 6, (2000), pp. 497–502.
28. W. J. Tomlinson and I. Collier, "The mechanical properties and microstructures of copper and brass joints soldered with eutectic tin–bismuth solder", *Journal of Materials Science*, **22**, 5, (1987), pp. 1835–1839.
29. Z. Mei and L. W. Morris Jr., "Characterization of eutectic Sn–Bi solder joints", *Journal of Electronic Materials*, **21**, 6, (1991), pp. 599–607.
30. C. H. Raeder, L. E. Felton, D. B. Knorr, G. B. Schmeelk, and D. Lee, "Microstructural evolution and mechanical properties of Sn–Bi based solders",

The Proceedings of the 15th International Electronic Manufacturing Technology Symposium, New York, NY, Oct. 4–6, 1993, IEEE/CHMT, (1993), pp. 119–127.

31. Z. Mei and H. Holder, "Thermal fatigue failure mechanism of 58Bi–42Sn solder joints", *Journal of Electronic Packaging*, **118**, 6, (1996), pp. 62–66.
32. F. Hua, M. Zequn, and J. Glazer, "Eutectic Sn–Bi as an alternative to Pb–free solders", *The Proceedings of the 48th Electronic Components and Technology Conference*, Seattle, WA, May 25–28, 1998, IEEE, (1998), pp. 277–283.
33. H. W. Miao and J. G. Duh, "Microstructure evolution in Sn–Bi and Sn–Bi–Cu solder joints under thermal aging", *Materials Chemistry and Physics,* **71**, 3, (2001), pp. 255–271.
34. "D5.1 Analysis of the current status of European lead–free soldering 2004", Germany, European Lead–Free Soldering Network, NMP2–CT–2003–505504, (2005), p. 22.
35. "NEMI group recommends tin/silver/copper alloy as industry standard for lead–free solder reflow in board assemblies", Press release on Jan. 24, 2000, http://www.inemi.org/cms/newsroom/PR/2000/PR012400.html, (14.7.2005).
36. *Metals Handbook, Volume 1 – Properties and Selection of Metals*, 8th ed., New York, 1961, American Society for Metals, p. 1300.
37. C. S. Barrett and T. B. Massalski, *Structure of Metals*, New York, 1960, McGraw–Hill, p. 654.
38. K.–I. Ishii, "Deformation twinning of tin singly crystals under impact loading", *Journal of the Physical Society of Japan*, **4**, 10, (1959), pp. 1315–1321.
39. B. A. Bilby and A. G. Crocker, "The theory of the crystallography of deformation twinning", *The Proceedings of the Royal Society of London – Series A*, **288**, 1413, (1965), pp. 240–255.
40. B. Chalmers, "The twinning of single crystals of tin", *The Proceedings of the Physical Society*, **47**, 4, (1935), pp. 733–746.
41. M. F. Ashby and D. R. H. Jones, *Engineering Materials – An Introduction to Their Properties and Applications*, Oxford, 1980, Pergamon Press, p. 278.

42. J. Weertman and J. R. Weertman, "Mechanical properties, strongly temperature dependent", in R. W. Cahn, *Physical Metallurgy*, Amsterdam, 1965, North–Holland Publishing Company, pp. 793–819.
43. G. E. Dieter, *Mechanical Metallurgy*, 3rd ed., New York, 1986, McGraw–Hill Book Company, p. 751.
44. W. G. Johnston and J. J. Gilman, "Dislocation velocities, dislocation densities, and plastic flow in lithium fluoride crystals", *Journal of Applied Physics*, **30**, 2, (1959), pp. 129–144.
45. J. J. Gilman and W. G. Johnston, "The origin and growth of glide bands in lithium fluoride crystals", in J. C. Fuisher, W. G. Jognston, R. Thomson, and T. Vreeland Jr., *Dislocations and Mechanical Properties of Crystals*, New York, 1956, Jonh Wiley & Sons, pp. 117–163.
46. A. L. Titchener and M. B. Bever, "The stored energy of cold work", *Progress in Metal Physics*, **7**, (1958), pp. 247–338.
47. W. F. Smith, *Principles of Materials Science and Engineering*, 2nd ed., New York, 1990, McGraw–Hill, p. 832.
48. D. Hardwick, C. M. Sellars, and W. J. McG. Tegart, "The occurrence of recrystallization during high–temperature creep", *Journal of the Institute of Metals*, **90**, (1961), pp. 21–22.
49. D. McLean and M. H. Farmer, "The relation during creep between grain–boundary sliding, sub–crystal size, and extension", *Journal of Institute of Metals*, **85**, (1956), pp. 41–50.
50. P. Gay and A. Kelly, "X–ray studies of polycrystalline metals deformed by rolling. II. Examination of the softer metals, tin, zinc, lead and cadmium", *Acta Crystallographica*, **6**, (1953), pp. 172–177.
51. A. G. Guy, *Elements of Physical Metallurgy*, 2nd ed., London, 1960, Addison–Wesley Publishing Company Inc., p. 528.
52. S. Terashima and M. Tanaka, "Thermal fatigue properties of Sn–1.2Ag–0.5Cu–xNi flip chip interconnects", *Materials Transactions*, **45**, 3, (2004), pp. 681–688.

53. S. Terashima, K. Takahama, M. Nozaki, and M. Tanaka, "Recrystallization of Sn grains due to thermal strain in Sn–1.2Ag–0.5Cu–0.05Ni solder", *Materials Transactions*, **45**, 4, (2004), pp. 1383–1390.
54. P. T. Vianco, J. A. Rejent, and A. C. Kilgo, "Time–independent mechanical and physical properties of the ternary 95.5Sn–3.9Ag–0.6Cu solder", *Journal of Electronic Materials*, **32**, 3, (2003), pp. 142–151.
55. P. Lauro, S. K. Kang, W. K. Choi, and D.–Y. Shih, "Effect of mechanical deformation and annealing on the microstructure and hardness of Pb–free solders", *Journal of Electronic Materials*, **32**, 12, (2003), pp. 1432–1440.
56. J. G. Byrne, *Recovery, Recrystallization, and Grain Growth*, New York, 1965, The MacMillan Company, p. 179.
57. R. W. Cahn, "Recovery and recrystallization", in R. W. Cahn, *Physical Metallurgy*, Amsterdam, 1965, North–Holland Publishing Company, pp. 925–987.
58. M. Avrami, "Kinetics of phase change. II Transformation–time relations for random distribution of nuclei", *Journal of Chemical Physics*, **8**, (1940), pp. 212–224.
59. S. S. Gorelik, *Recrystallization in Metals and Alloys*, Moscow, 1978, MIR Publishers, p. 479.
60. W. C. Leslie, T. J. Michalak, and F. W. Aul, "The annealing of cold–worked iron", in C. W. Spencer and F. E. Werner, *Iron and Its Dilute Solid Solutions*, New York, 1963, Interscience Puhlishers, pp. 103-119.
61. P. Adeva, G. Caruana, O. A. Rauno, and M. Torralba, "Microstructure and high temperature mechanical properties of tin", *Materials Science and Engineering – A*, **194**, 1, (1995), pp. 17–23.
62. C. Andersson, Z. Lai, J. Liu, H. Jiang, and Y. Yu, "Comparison of isothermal mechanical fatigue properties of lead–free solder joints and bulk solders", *Materials Science and Engineering – A*, **394**, 1–2, (2005), pp. 20–27.
63. J. Zhao, Y. Mutoh, Y. Miyashita, and S. L. Mannan, "Fatigue crack–growth behavior of Sn–Ag–Cu and Sn–Ag–Cu–Bi lead–free solders", *Journal of Electronic Materials*, **31**, 8, (2002), pp. 879–886.

64. Y. Mutoh, J. Zhao, Y. Miyashita, and C. Kanchanomai, "Fatigue crack growth behaviour of lead–containing and lead–free solders", *Soldering and Surface Mount Technology*, **13**, 3, (2002), pp. 37–45.
65. J. Zhao, Y. Miyashita, and Y. Mutoh, "Fatigue crack growth behavior of 96.5Sn–3.5Ag lead–free solder", *International Journal of Fatigue*, **23**, 8, (2001), pp. 723–731.
66. S. Terashima and M. Tanaka, "Thermal fatigue of Sn–1.2Ag–0.5Cu–xNi flip chip interconnections", *Materials Transactions*, **45**, 3, (2004), pp. 681–688.
67. C. F. Coombs Jr., *Printed Circuits Handbook*, 5th ed., New York, 2001, McGraw–Hill, p. 1200.
68. Y. S. Touloukian and C. Y. Ho, *Thermal Expansion: Metallic Elements and Alloys*, New York, 1975, IFI/Plenum, p. 316.
69. P. M. Hall, "Forces, moments, and displacements during thermal chamber cycling of leadless ceramic chip carriers soldered to printed boards", *IEEE Transactions on Components, Hybrids, and Manufacturing Technology*, **7**, 4, (1984), pp. 314–327.
70. W. J. Plumbridge, C. R. Gagg, and S. Peters, "The creep of lead–free solders at elevated temperatures", *Journal of Electronic Materials*, **30**, 9, (2001), pp. 1178–1183.
71. C.–K. Lin and D.–Y. Chu, "Creep rupture of lead–free Sn–3.5Ag and Sn–3.5Ag–0.5Cu solders", *Journal of Materials Science: Materials in Electronics*, **16**, 6, (2005), pp. 355–365.
72. M. Amagai, M. Watanabe, M. Omiya, K. Kishimoto, and T. Shibuya, "Mechanical characterization of Sn–Ag–based lead–free solders", *Microelectronics Reliability*, **42**, 6, (2002), pp. 951–966.
73. W. J. Plumbridge, R. J. Matela, and A. Weswater, *Structural Integrity and Reliability in Electronics*, Dordrecht, 2003, Kluwer Academic Publishers, p. 336.
74. IEC 60068–2–14 Ed. 5.0 b: 1984, "Environmental testing – part 2: tests. Test N: change of temperature", International Electrotechnical Commission, (1984), p. 34.
75. W. Q. Peng, "Lead–free electronic assembly based on Sn–Ag–Cu solders", Espoo, licentiate theses, Helsinki University of Technology, (2001), p. 124.

76. P. Marjamäki and J. K. Kivilahti, "Comparison between large amplitude vibration test and drop test", (submitted to *IEEE Transactions on Components and Packaging Technologies*, 2005).
77. K.–W. Moon, W. J. Boettinger, U. R. Kattner, F. S. Biancaniello, and C. A. Handwerker, "Experimental and thermodynamic assessment of Sn–Ag–Cu solder alloys", *Journal of Electronic Materials*, **29**, 10, (2000), pp. 1122–1136.
78. A. J. Schwartz, M. Kumar, and R. L. Adams, *Electron Backscatter Diffraction in Materials Science*, New York, 2000, Kluwer Academic / Plenum Publishers, p. 339.
79. JESD22–B111, "Board level drop test method of components for handheld electronic products", JEDEC Solid State Technology Association, 2003, p. 16.
80. IEC 91/530/NP, "Surface mounting technology – Environmental and endurance test methods for surface mount solder joint. Part 3: cyclic drop test", International Electrotechnical Commission, proposal (26.9.2005), p. 14.
81. T. O. Reinikainen, P. Marjamäki, and J. K. Kivilahti, "Deformation characteristics and microstructural evolution of SnAgCu solder joints", *The Proceedings of the 6th EuroSimE Conference*, Berlin, Germany, April 18–20, 2005, IEEE, (2005), pp. 91–98.
82. R. Nikander, "Characterization of the mechanical properties of the dilute tin based solder alloys", Espoo, master's theses, Helsinki University of Technology, (1999), p. 79.
83. T. Reinikainen and J. K. Kivilahti, "Deformation behavior of dilute SnBi(0.5 to 6 at. pct) solid solutions", *Metallurgical and Materials Transactions A*, **30**, (1999), pp. 123–132.
84. D. C. Montgomery, *Design and Analysis of Experiments*, 5th ed., New York, 2001, John Wiley & Sons, p. 672.
85. *Engineering Statistics Handbook*, NIST/SEMATECH e–Handbook of Statistical Methods, http://www.itl.nist.gov/div898/handbook/, (20.1.2005).
86. E. L. Lehmann, *Nonparametric Statistical Methods Based on Ranks*, New York, 1975, McGraw–Hill, p. 787.

87. MIL–STD–721C, "Definition of terms for reliability and maintainability", The United States Department of Defense, (1981), p. 14.
88. W. Weibull, "A statistical theory of the strength of materials", *Ingeniörsvetenskapsakademiens Handlingar*, **151**, (1939), pp. 1–45.
89. W. Weibull, "A statistical distribution function of wide applicability", *Journal of Applied Mechanics*, **18**, 9, (1951), pp. 293–297.
90. F. Jensen, *Electronic Component Reliability*, Chichester, 1995, John Wiley & Sons, p. 355.
91. P. D. T. O'Connor, *Practical Reliability Engineering*, Chichester, 1998, John Wiley & Sons, p. 431.